Journal of Catalysis 389 (2020) 382–399

Contents lists available at ScienceDirect

Journal of Catalysis

journal homepage: www.elsevier.com/locate/jcat

Promoting effect of Cu-doping on catalytic activity and SO_2 resistance of porous CeO_2 nanorods for H_2S selective oxidation

Xiaohai Zheng [a], Yanli Li [b], Shijing Liang [a,*], Zheng Yao [a], Yong Zheng [a], Lijuan Shen [a,*], Yihong Xiao [a], Yongfan Zhang [b], Chaktong Au [a], Lilong Jiang [a,*]

[a] National Engineering Research Center of Chemical Fertilizer Catalyst, Fuzhou University, Fuzhou, Fujian 350002, People's Republic of China
[b] College of Chemistry, Fuzhou University, Fuzhou, Fujian 350116, People's Republic of China

ARTICLE INFO

Article history:
Received 18 February 2020
Revised 4 June 2020
Accepted 7 June 2020
Available online 20 June 2020

Keywords:
CeO_2
Cu doping
Oxygen vacancies
Density functional theory calculations
H_2S selective oxidation

ABSTRACT

A facile procedure for doping copper species into CeO_2 lattices to prevent ceria from being deactivated and to offer additional active sites for selective H_2S oxidation is reported here. Among the prepared catalysts, porous 10Cu/Ce nanorods with well-defined (100) and (110) reactive planes display excellent catalytic performance, exhibiting H_2S conversion and sulfur selectivity of 100% at 220 °C, which is higher than those of most reported Ce-based catalysts. More importantly, electron transfer from Cu^+ to Ce^{4+} suppresses the transfer of electrons from SO_2 to Ce^{4+}, leading to inhibition of SO_2 oxidation to surface sulfate, which could deactivate the catalyst. Overall, the results of systematic experimental and theoretical studies prove that copper doping effectively promotes the formation of oxygen vacancies and resistance against SO_2 poisoning. Furthermore, through in situ diffuse reflection infrared Fourier transform spectroscopy investigation and density functional theory calculations, the reaction intermediates in selective H_2S oxidation and mechanism of SO_2 resistance over the Cu-doped CeO_2 catalysts are revealed.

1. Introduction

Nowadays, the rapid development of industrial processes has accelerated the combustion of fossil fuels and increased H_2S emission, inevitably causing severe environmental problems [1,2]. Industrially, the Claus process is the most extensively applied technique to eliminate H_2S while recovering elemental sulfur (S) [3]. However, because of thermodynamic constraints, around 4% of H_2S is left in the tail gas. To comply with ever tightening environmental regulations, advanced technologies have been developed to lower H_2S emissions. Among them, the selective oxidation process ($H_2S + 1/2O_2 \rightarrow S_n + H_2O$) is attractive because H_2S can be converted completely to sulfur [4].

With excellent oxygen storage capacity, versatile acid–base catalytic chemistry, and superior redox properties, ceria (CeO_2) has received intensive attention in the catalytic domain of environmental pollution control [5]. Recently, CeO_2 has been applied as a desirable catalyst for H_2S selective oxidation [6]. For instance, Palma and co-workers attributed the effective conversion of H_2S to sulfur over CeO_2-supported vanadium catalysts to the synergic effect of V_2O_5 and CeO_2 [7]. Furthermore, Koyuncu et al. reported improved H_2S conversion over Ce–Fe catalysts and related the enhanced redox ability of the catalysts to the presence of a Ce^{3+}/Ce^{4+} redox cycle [8]. Recently, we disclosed that CeO_2 nanorods with well-defined (100) and (110) planes facilitate promoted catalytic activity for H_2S selective oxidation [9]. Based on the results of experimental and theoretical investigations, high H_2S conversion and sulfur selectivity are related to the abundant presence of oxygen vacancies, which can be tuned through the control of catalyst nanocrystal facets. Nonetheless, the long-term stability of the developed CeO_2-based catalysts is unsatisfactory because the SO_2 produced in side reactions ($S + O_2 \rightarrow SO_2$, $H_2S + 3/2O_2 \rightarrow SO_2 + H_2O$) reacts with ceria to form sulfate species, resulting in blockage of pores and active sites.

Doping and introducing additives are effective ways to improve the sulfur resistance of Ce-based catalysts, as demonstrated in a number of applications [10]. Previous studies have revealed that the incorporation of transition metals such as Mn, Zr, and Nb into a CeO_2 lattice would create a new redox cycle with the concomitant reduction of surface cerium ($Ce^{4+} \leftrightarrow Ce^{3+}$) as a result of electron unsaturation of the *d* orbits [11]. The created redox cycle induces preferential interaction of SO_2 with the transition metal, consequently avoiding the cerium active sites being poisoned. Compared with those of bulk metal oxides, the metal ions dis-

* Corresponding authors.
E-mail addresses: sjliang2012@fzu.edu.cn (S. Liang), syhgslj@fzu.edu.cn (L. Shen), jll@fzu.edu.cn (L. Jiang).

https://doi.org/10.1016/j.jcat.2020.06.010
0021-9517/

Nomenclature

*	active site	r_{s0}	initial desulfurization rate
A	pre-exponential factor	T	temperature, K
[A]	concentration of A, mol/m^3	W_s	mass of the formed sulfur, mg
E_a	activation energy, J/mol	t	time, min
K_s	equilibrium constant, Pa^{-1}	α	a parameter related to saturated sulfur capacity
k_s	reaction rate constant	Φ_s	function of sulfur deposition
R	gas constant, 8.314 J/(mol·K)		

persed in a CeO_2 lattice are also more stable. However, it is rare to come across studies on SO_2 tolerance of CeO_2 in selective H_2S oxidation.

In the present work, Cu-doped CeO_2 porous nanorods with clearly defined reactive facets were successfully prepared by a simplified hydrothermal process. The obtained *x*Cu/Ce catalysts exhibit excellent H_2S conversion, sulfur selectivity, and long-term stability. We employed advanced characterization techniques to gain insight into the impact of copper doping on the surface chemistry and structural defects of porous CeO_2 nanorods. Moreover, the structure–activity relationships of the Cu-doped CeO_2 catalysts for enhancement of catalytic performance in H_2S selective oxidation are discussed. It was observed that Cu doping weakens SO_2 adsorption on ceria and the *x*Cu/Ce catalysts are more resistant to deactivation induced by SO_2. In addition, we applied in situ diffuse reflection infrared Fourier transform spectroscopy (DRIFTS) investigation and theoretical calculations to identify the reaction intermediates in H_2S selective oxidation and to study the nature of SO_2 resistance over Cu-doped CeO_2. It is anticipated that the outcomes of this work could provide useful guidelines for the development of highly effective desulfurization catalysts.

2. Experimental

2.1. Preparation of catalysts

Typically, 16 mmol of $Ce(NO_3)_3{\cdot}6H_2O$ and a calculated amount of $Cu(NO_3)_2{\cdot}3H_2O$ were dissolved in distilled water (10 mL) at 25 °C, followed by the addition of 0.1 g urea and 10 mmol of polyvinylpyrrolidone k-30 (PVP). After that, 10 mL of $NH_3{\cdot}H_2O$ solution was added dropwise into the above solution and stirred vigorously for 40 min. Subsequently, the homogenous solution was moved into a 100 mL Teflon-lined stainless steel autoclave to undergo thermal treatment at 100 °C for 24 h. The obtained solid samples were immersed in NaOCl solution (5000 ppm) for 2 h and then washed three times with absolute ethyl alcohol and distilled water, dried overnight at 80 °C, and calcined in air at 500 °C for 2 h. The as-harvested catalysts are labeled here as *x*Cu/Ce (where x = 5, 10, and 15 when Cu/(Cu + Ce) = 0.05, 0.10, and 0.15, respectively). The undoped catalyst is denoted as CeO_2.

2.2. Characterization

The structural information for the as-prepared *x*Cu/Ce samples was characterized using an X'Pert3 diffractometer with Cu*K*a α source (λ = 0.15405 nm) operating at 40 mA and 45 kV. The texture parameters of samples were determined by N_2 sorption measurements at −196 °C employing a 3Flex analyzer (U.S. Micromeritics). The scanning electron microscopic (SEM) micrographs were taken over a Hitachi S-4800 instrument with energy-dispersive X-ray (EDX) spectroscopy. Raman spectra were recorded under ambient conditions on a Renishaw Raman spectrometer equipped with a laser beam of λ = 532 nm. Inductively coupled plasma optical emission spectrometry (ICP-OES) was conducted on a Perkin–Elmer Optima 8000 to analyze the concentrations of Cu and Ce. Transmission electron microscopy (TEM) and high-resolution TEM (HRTEM) coupled with selected area electron diffraction (SAED) and energy-dispersive X-ray spectrometry (EDX) was conducted with a Tecnai G^2 F20 Spirit microscope operated at 200 kV. Electron paramagnetic resonance (EPR) analysis was performed by a Bruker E-500 spectrometer at 25 °C and 100 kHz. The samples were characterized by X-ray photoelectron spectroscopy (XPS) as well as X-ray-excited Auger electron spectroscopy (XAES; Thermo Escalab250, XPS). The electron binding energies (BE) were calibrated using the C1*s* line of adventitious carbon (284.6 eV).

N_2O chemisorption, H_2 temperature-programmed reduction (H_2-TPR), and CO_2 and O_2 temperature-programmed desorption–mass spectrometry (CO_2-TPD-MS and O_2-TPD-MS) profiles were generated using an AutoChem 2920 instrument (Micromeritics) equipped with a thermal conductivity detector (TCD) and a Hiden HPR-20 mass spectrometer. Prior to N_2O chemisorption, 0.1 g of sample was reduced in 10% H_2/Ar at 300 °C for 1 h. The consumption of N_2O and the release of N_2 ($2Cu + N_2O \rightarrow N_2 + Cu_2O$) were recorded at a sample temperature of 60 °C. Before a H_2-TPR run, the catalyst (100 mg) was pretreated with a He flow (30 mL/min) at 300 °C for 1 h and cooled to 25 °C. The TPR profiles were recorded upon treating the samples from 50 to 900 °C in a 10 vol % H_2/Ar flow (30 mL/min) at a 10 °C/min ramp. In CO_2-TPD-MS experiments, the pretreatment process of heating in an Ar flow at 300 °C for 1 h and cooling down to 25 °C was also carried out. Then pure CO_2 gas was fed to the reactor at 25 °C for 1.5 h and the CO_2 desorption profiles were recorded under Ar flow from 50 to 900 °C (10 °C/min). As for O_2-TPD-MS experiments, the pretreated sample was exposed to an O_2 flow (30 mL/min) at 30 °C. Then O_2 desorption was monitored with the increase of the sample temperature from 30 to 900 °C in a He flow (30 mL min^{-1}).

In situ DRIFTS was conducted on a Nicolet-6700 FTIR instrument with a mercury–cadmium–tellurium (MCT) detector, adopting 64 scans at 2 cm^{-1} resolution. Prior to measurement, the sample was heated to 300 °C in a helium flow for 0.5 h to remove surface impurities. As for CO adsorption, the background spectrum was collected after cooling down to 30 °C. Afterward, a stream of 1 vol% CO/He was introduced into the reactor for 1 h and a spectrum was recorded. The adsorption studies were performed by recording the spectra at designated temperatures (100 and 150 °C). For H_2S and O_2 co-adsorption, the background spectrum was collected at 100 °C. Then the sample was exposed to 5000 ppm H_2S and 2500 ppm O_2 in helium, and a DRIFTS spectrogram was recorded. The above procedure was repeated and the spectra were recorded at 130, 160, 190, 220, and 250 °C.

2.3. Catalytic performance measurement

Selective oxidation of H_2S was tested over a continuous-fed microreactor at atmospheric pressure (Fig. S1 in the Supplementary Material). Typically, a portion of sifted catalyst (0.2 g, 20–60 mesh) was securely positioned in the reactor. The reactant flow

contained 2500 ppm O_2, 5000 ppm H_2S, and balance N_2 at a rate of 35 mL min^{-1}, which was directed into the reactor at a weight hourly space velocity (WHSV) of 10 500 $mL{\cdot}g^{-1}{\cdot}h^{-1}$ as the reaction temperature increased from 100 to 250 °C. The gases were analyzed by a gas chromatograph (GC-9720) equipped with a sulfur-resistant column (polytetrafluoroethylene tube) and a thermal conductivity detector (TCD). Prior to the test, the catalyst was subjected to preadsorption operation at low temperature for H_2S adsorption and desorption equilibrium of both catalyst and GC. A condenser was attached to the effluent side of the reactor to trap produced sulfur. The H_2S conversion (X_{H2S}), sulfur selectivity (S_{sulfur}), and sulfur yield are defined as follows:

$$X_{H_2S} = \frac{[H_2S]_{in} - [H_2S]_{out}}{[H_2S]_{in}} \times 100\%, \quad (1)$$

$$S_{sulfur} = \frac{[H_2S]_{in} - [H_2S]_{out} - [SO_2]_{out}}{[H_2S]_{in} - [H_2S]_{out}} \times 100\%, \quad (2)$$

$$\text{Sulfur yield} = [X_{H_2S}] \times [S_{sulfur}] \times 100\%. \quad (3)$$

As for the tests performed at high WHSV (42 000 $mL{\cdot}g^{-1}{\cdot}h^{-1}$) to rule out external/internal diffusion effects, the reaction rate (r_{H2S}) of H_2S oxidation is calculated according to the following formula:

$$r_{H_2S} = \frac{X_{H_2S} \times C_0 \times V_{gas}}{m_{cat.}} (\text{mol} \cdot g_{cat.}^{-1} \cdot s^{-1}). \quad (4)$$

Here, X_{H_2S} is the conversion of H_2S at 220 °C, r_{H_2S} stands for the reaction rate in $mol{\cdot}g_{cat.}^{-1}{\cdot}s^{-1}$, $m_{cat.}$ means the catalyst weight in grams, and V_{gas} and C_0 are the total molar flow rate and H_2S concentration in the inlet gas.

The turnover frequency (TOF) is determined using the expressions

$$TOF_{Cu} = \frac{X_{H_2S} \times C_0 \times V_{gas} \times M_{Cu}}{m_{cat.} \times D \times \beta_{Cu}} (s^{-1}), \quad (5)$$

$$TOF_{Ce} = \frac{X_{H_2S} \times C_0 \times V_{gas}}{n_{CeO_2}} (s^{-1}), \quad (6)$$

where D is the Cu dispersion, M_{Cu} is the molar weight of Cu (63.546 $g{\cdot}mol^{-1}$), n_{CeO2} is the molar mass of CeO_2, and β_{Cu} is the copper content (g_{Cu}/g_{cat}).

2.4. DFT calculations

2.4.1. Computation method

All spin-polarized DFT calculations were performed using the Vienna *ab initio* simulation package (VASP), and the interactions between electrons and ions were described by employing the projector augmented wave (PAW) method [12]. The exchange-correction functions were described based on the Perdew–Burke–Ernzerhof generalized gradient approximation (PBE-GGA) with a 450 eV cut-off energy. The strong Coulomb interaction of localized Cu3*d* and Ce4*f* electrons were corrected by PBE plus an on-site repulsion U (PBE + U) approach. We adopted values of U_{eff} = 4.5 eV and 5.0 eV for Ce and Cu atoms in this study, respectively. The convergence thresholds of the maximum force and energy change were set to 0.03 eV/Å and 10^{-5} eV, respectively. In addition, the Γ point was used to sample the Brillouin zone integration.

2.4.2. Surface model

As shown in Fig. S2A, ceria possesses a cubic fluorite structure with eight oxygen and four cerium ions per unit cell. We constructed a stoichiometric CeO_2 (110) surface with a six-layer slab and an (11.592 Å × 10.929 Å) supercell (Fig. S2B). The vacuum of 12 Å between the adjacent slabs was used to separate adjacent slabs from interactions and the reduced ceria surface was optimized via removing an O atom from the top layer.

The adsorption energy (E_{ad}) was calculated by the equation $E_{ad} = E_{(Ce1\text{-}xMxO2\text{-}\delta\ +\ adsorbate)} - E_{(Ce1\text{-}xMxO2\text{-}\delta)} - E_{(adsorbate)}$. Here, $E_{(Ce1\text{-}xMxO2\text{-}\delta\ +\ adsorbate)}$ represents the total energy of reduced pristine or Cu-doped CeO_2 surface with adsorbate. $E_{(Ce1\text{-}xMxO2\text{-}\delta)}$ and $E_{(adsorbate)}$ are the energies of the pristine or Cu-doped CeO_2 surface and a neutral adsorbate, respectively. Thus, a positive E_{ad} value means endothermic adsorption, whereas a negative one means exothermic adsorption. That is, the more negative values of E_{ad} indicate stronger adsorption.

3. Results and discussions

3.1. Structural properties and morphological characteristics

The XRD patterns of *x*Cu/Ce catalysts are presented in Fig. 1A. The diffraction peaks of undoped CeO_2 at 2θ = 28.6°, 33.3°, 47.5°, 56.3°, 59.2°, 69.2°, 76.3°, and 79.2°, are assigned to the (111), (200), (220), (311), (222), (400), (331), and (420) crystal faces of fluorite-type CeO_2 (JCPDS 34-0394, *Fm*3*m*) with face-centered cubic (FCC) crystal structure [13]. For the samples with low Cu content (5Cu/Ce and 10Cu/Ce), no peaks ascribable to CuO phases were found. The absence of CuO peaks implies that the copper species are incorporated into the CeO_2 matrix with the formation of a solid solution and/or highly dispersed on the ceria surface. Over 15Cu/Ce, there are two peaks at 35.6° and 38.9° assignable to the $(\bar{1}11)$ and (111) planes of the CuO phase (JCPDS 45-0937). The detection of CuO suggests that with excess copper doping, not all the copper can incorporate into the CeO_2 lattice, and there is formation of CuO nanoparticles. Since the copper ion radius is smaller than that of the cerium ion, the (111) peaks of Cu-doped CeO_2 show a continuous shift to higher Bragg angles resulting from increased copper incorporation into the CeO_2 lattice (Fig. S3). According to the oxygen vacancy formation theory, the doping of copper ions into the CeO_2 crystal lattice would enhance the formation of oxygen vacancies for the maintenance of electroneutrality [14]. The cell parameters of the *x*Cu/Ce catalysts were calculated as summarized in Table 1. That the cell parameters decrease with increasing Cu content also evinces that the copper could be partly substituted into the ceria lattice with the formation of CuO–CeO_2 solid solution. Moreover, the plot of lattice parameter versus copper content gives a linear fitting, as suggested by Vegard's law (Fig. 1B) [15]. The results in Table 1 show that the crystallite sizes of the Cu-doped CeO_2 samples are smaller than that of CeO_2, mainly due to the suppression of crystallite growth as a result of Cu incorporation. When the copper content is 15 mol.%, the aggregation of Cu species on the CeO_2 surface results in crystals of larger size. In addition, with the increase in Cu content, the intensity of the (111) peak decreases, indicating gradual deterioration of crystallinity across the *x*Cu/Ce samples.

It has been accepted that oxygen vacancies are the main defects of ceria, which play an important role in catalytic reactions. Raman spectroscopy was conducted to probe the crystal defects in the form of oxygen vacancies over CeO_2-based catalysts. It is clearly observed from Fig. 1C that all the copper–ceria catalysts display a symmetrical band at ca. 461 cm^{-1}, which is attributable to the triply degenerate F_{2g} symmetry vibration mode of CeO_2 [16]. Clearly, the F_{2g} band of the *x*Cu/Ce catalysts gradually broadens and weakens as well as exhibiting a shift toward lower wavenumber with the increase of Cu content. The red shift of the F_{2g} band could be related to lattice shrinkage caused by the introduction of copper cations into the ceria lattice [17], as evidenced by the XRD results. In addition, the *x*Cu/Ce samples show weak bands at around 598 and 256 cm^{-1}, which are ascribable to the Frenkel-

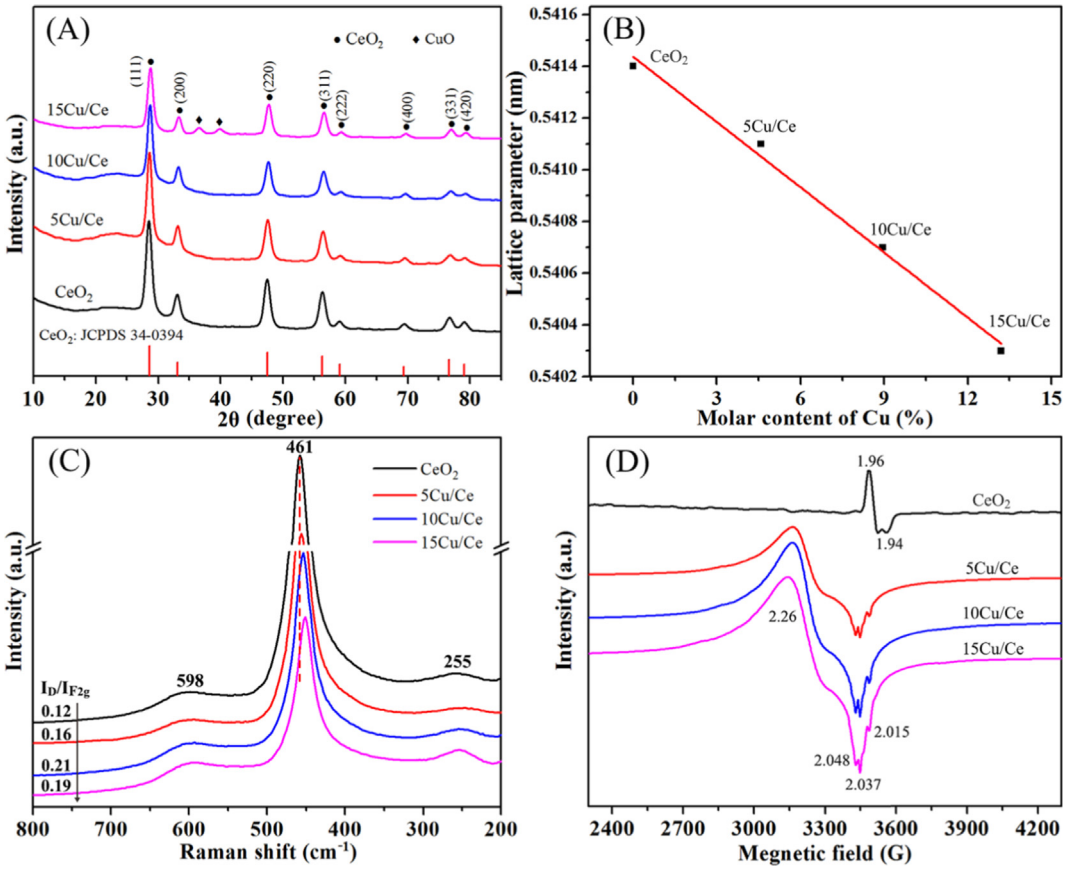

Fig. 1. (A) XRD pattern, (B) relationship between cell parameter and Cu doping content, (C) Raman spectra, and (D) EPR spectra of as-synthesized CeO_2 and *x*Cu/Ce catalysts.

Table 1
Structural and textural parameters of the CeO_2 and *x*Cu/Ce catalysts.

Samples	$n_{(Cu)}/n_{(Cu+Ce)}$ (%)[a]	Lattice parameter (nm)[b]	Crystal size (nm)[c]	Crystallinity (%)	Surface area (m^2/g)	Pore volume (cm^3/g)	Average pore size (nm)
CeO_2	–	0.5414	9.2	86.5	74.9	0.45	8.90
5Cu/Ce	4.58	0.5411	8.8	72.6	82.5	0.53	9.80
10Cu/Ce	8.95	0.5407	8.3	68.9	97.8	0.56	10.7
15Cu/Ce	13.2	0.5403	8.6	65.3	84.7	0.48	8.50

[a] Cu concentration determined by ICP-OES.
[b] For fluorite phase.
[c] Calculated from (111) plane using the Scherrer equation.

type anion defects (D) and second-order transverse acoustic modes (2TA), respectively. The latter could be related to the move of an oxygen ion from a lattice position to an interstitial position, creating a defect at the interstitial site and a vacancy at the initial position [18]. It is noted that the wavenumber difference between F_{2g} and oxygen defect bands is about 137 cm^{-1}, indicating that oxygen vacancies in the copper–ceria samples originate from internal defects (conversion of Ce^{4+} to Ce^{3+}). In Raman investigation, the peak intensity ratio (i.e., I_D/I_{F2g}) was calculated to estimate the concentration of oxygen vacancy in CeO_2 materials: the higher the I_D/I_{F2g} ratio, the larger the number of surface oxygen vacancies [19]. It is observed that over the prepared CeO_2 materials the I_D/I_{F2g} ratios follow the order 10Cu/Ce (0.21) > 15Cu/Ce (0.19) > 5Cu/Ce (0.16) > CeO_2 (0.12), suggesting that the incorporation of Cu species is favorable for forming oxygen vacancies ($Ce^{4+} + O^{2-} + Cu^{2+} \leftrightarrow Ce^{3+} + V_{ö} + Cu^{+} + O$, where $V_{ö}$ is a doubly ionized oxygen vacancy, O^{2-} and O represent the lattice oxygen and removed oxygen, respectively) due to the strong interaction between Cu species and CeO_2. In addition, the oxygen vacancies would lead to lattice distortion and charge imbalance of CeO_2, thus creating more active sites on the surface of catalyst for higher adsorption of O_2 molecules, which is beneficial to selective oxidation of H_2S. To further verify the variation trend of oxygen vacancy concentration, the defect concentration of CeO_2 materials was estimated based on Raman measurements. First, the grain size (d_g) was calculated according to the following equation as presented by Trogadas et al.: $\Gamma(cm^{-1}) = 51.8/d_g + 5$ (nm), where Γ stands for half-width at half-maximum (HWHM) of the F_{2g} band in Raman spectra [20]. Then the average length (L) between two lattice defects is determined using the expression $L\,(nm) = \sqrt[3]{(\alpha/2d_g)^2[(d_g - 2\alpha)^3 + 4{d_g}^2\alpha]}$, where α means the radius of the ceria cell (0.34 nm). Finally, the oxygen vacancy concentration N (cm^{-3}) is calculated by the following formula: $N = 3/(4\pi L^3)$ [21]. The acquired d_g and O-vacancy concentration of *x*Cu/Ce catalysts derived from Raman data are summarized in Table S1. It is apparent that the grain sizes are 8–10 nm, which match well with the crystallite sizes acquired from XRD by utilizing the Scherrer

formula. In addition, the concentration of oxygen vacancies in *x*Cu/Ce increases nonmonotonically with increased copper content, with 10Cu/Ce being the highest among the four catalysts in oxygen vacancy concentration. 15Cu/Ce possesses lower concentrations of oxygen vacancies due to the covering of the oxygen vacancy sites by aggregated CuO nanoparticles.

EPR analyses were conducted to evidence the formation of oxygen vacancies, and the results are shown in Fig. 1D. The pristine CeO_2 exhibits two signals at $g_{//}$ = 1.94 and $g_{\perp}$ = 1.96 corresponding to Ce^{3+} ions in the CeO_2 matrix [22]. For the 5Cu/Ce sample, a broad signal with a 100 G linewidth located at g_{av} = 2.26 could be ascribed to a nanoscale 2D structure formed by dipolar interaction of isolated Cu^{2+} ions [23]. The signals at $g_{//}$ = 2.037 and $g_{\perp}$ = 2.015 are ascribed to O^{2-} species bound to Ce^{4+} cations (O^{2-}–Ce^{4+}). One additional signal at g = 2.048 is related to oxygen vacancies and Ce^{3+} ions [24]; its intensity increases with the rise of Cu content, suggesting an increase in oxygen vacancies. Notably, the peak intensity of g_{av} = 2.26 increases with the increase of Cu content from 5 to 10 mol.%, which suggests the generation of more isolated Cu^{2+} ions in CeO_2. As for 15Cu/Ce, the g_{av} = 2.26 signal intensity remains almost the same as that of the 10Cu/Ce sample, implying that the excess copper species exists as bulk CuO particles on the catalyst surface, in accordance with the XRD spectra showing the presence of CuO particles on the 15Cu/Ce sample. In addition, the oxygen signal at g = 2.048 observed over 15Cu/Ce is weaker than that over 10Cu/Ce, indicating that an excess amount of Cu species would inhibit the formation of oxygen vacancies. The EPR results verify that the incorporation of a moderate amount of copper species could optimize the formation of oxygen vacancies, which is in accordance with the results of Raman analysis.

XPS analyses were carried out to characterize the surface composition and chemical nature of elements on the copper–ceria catalysts. As shown in Fig. 2A, Ce3*d* always shows relatively complex features because of the fractional occupancy of the valence 4*f* orbitals and hybridization with ligand orbitals. As reported, eight spin–orbit components are acquired by multiplet splitting. The two series of spin–orbital multiplets labeled as *v* and *u* are related to $3d_{5/2}$ and $3d_{3/2}$ contributions, respectively. In detail, the bands denoted as *u*′ (902.8 eV) and *v*′ (884.6 eV) are characteristic of the $3d^{10}4f^{1}$ initial electronic state of Ce^{3+}, while the bands labeled as *u* (901.3 eV) and *v* (882.1 eV), *u*″ (907.5 eV) and *v*″ (889.5 eV), and *u*‴ (916.8 eV) and *v*‴ (898.3 eV) are considered as the fingerprints of Ce^{4+} species (in the $3d^{10}4f^{0}$ electronic state) [25]. The presence of Ce^{3+} is ascribed to the strong interaction between CeO_2 and copper species that facilitate the electron transfer process "$Cu^{+} + Ce^{4+} \leftrightarrow Cu^{2+} + Ce^{3+}$." The existence of Ce^{3+} ions could also trigger charge imbalance and thereby create unsaturated chemical bonds and vacancies, leading to the enhancement of chemisorbed oxygen on the catalyst surface. The proportion of Ce^{3+} species is calculated using a semiquantitative method of integrated peak areas according to the formula $Ce^{3+}\ (\%) = \frac{S_{u'}+S_{v'}}{\sum(S_u+S_v)} \times 100$, and the results are shown in Table S2. The percentages of Ce^{3+} ions are highly dependent on the Cu content. Among the *x*Cu/Ce catalysts, 10Cu/Ce exhibits the highest proportion of Ce^{3+} ions. It is accepted that the Ce^{3+} percentage is directly related to the concentration of oxygen vacancies because oxygen vacancies are formed through the reduction of Ce^{4+} to Ce^{3+}. Among the *x*Cu/Ce samples, 10Cu/Ce possesses the highest concentration of oxygen vacancies, dovetailing with the results of Raman and EPR analyses. The ample oxygen vacan-

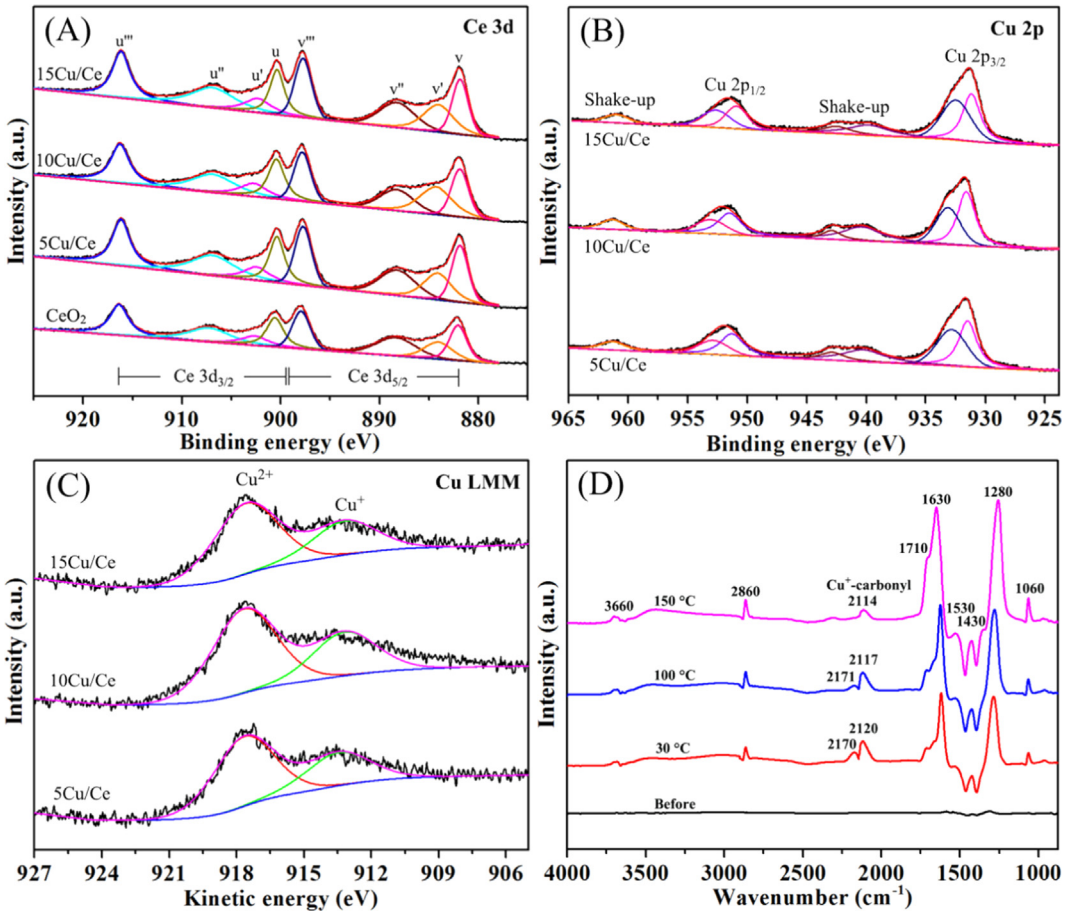

Fig. 2. (A) XPS Ce3*d* spectra, (B) XPS Cu2*p* spectra, and (C) Cu LMM Auger spectra of as-synthesized CeO_2 and *x*Cu/Ce catalysts; (D) in situ DRIFTS spectra of CO adsorption over 10Cu/Ce recorded at different temperatures.

cies are highly conducive to the transformation of adsorbed oxygen to reactive oxygen species as well as to the diffusion of lattice oxygen from the bulk to the surface to participate in the redox reactions (i.e., $H_2S + O_{latt} \rightarrow S + H_2O + O_{vac}$; $O_2 + 2O_{vac} \rightarrow 2O_{latt}$) [26]. It is hence deduced that the doping of copper ions into ceria is favorable for the increase of oxygen vacancies in the *x*Cu/Ce catalysts.

The O1*s* profiles of the *x*Cu/Ce catalysts are fitted with two Gaussian peaks as presented in Fig. S4. The peak at ca. 528.8 eV denoted as O_{latt} is ascribed to surface lattice oxygen of CeO_2, and the shoulder peak at around 531.9 eV is ascribed to chemisorbed oxygen species (O_{ad}), including weakly bonded oxygen (O_2^{2-} and O^-), hydroxyl, or adsorbed water on the surface [27]. It is accepted that the adsorbed oxygen species with higher mobility are active in the oxidative reaction, and thus the relatively high O_{ad} proportion ($O_{ad}/(O_{ad} + O_{latt})$) would reflect the reaction rates over the *x*Cu/Ce catalysts. It is observed from Table S2 that the O_{ad} quantity shows an order of 10Cu/Ce > 15Cu/Ce > 5Cu/Ce > CeO_2, in a perfect match with that of Ce^{3+} quantity. The phenomena suggest that Ce^{3+} has the ability to activate and transfer oxygen. With a high concentration of surface chemisorbed oxygen, the 10Cu/Ce sample is high in oxygen mobility, in agreement with its promising catalytic activity in H_2S selective oxidation.

The Cu2*p* spectra of the *x*Cu/Ce samples are illustrated in Fig. 2B. The Cu2$p_{1/2}$ and Cu2$p_{3/2}$ signals are at 954.0 eV and 934.1 eV, showing shake-up satellite peaks at 943–945 eV and 963 eV, respectively. These peaks are characteristics of Cu^{2+} species. Additionally, the low Cu2$p_{3/2}$ signal at 932.1 eV and the absence of a shake-up peak is attributed to the presence of Cu^+ species [28]. The existence of Cu^+ species is explained by the occurrence of the redox equilibrium (i.e., $Ce^{3+} + Cu^{2+} \leftrightarrow Ce^{4+} + Cu^+$) caused by the CuO_x–CeO_2 interaction. It is suggested that Cu^+ could be stabilized in the *x*Cu/Ce catalysts by the formed solid solution. Besides, Cu^+ is more easily substituted into the ceria lattice, since the radius of Cu^+ (0.096 nm) is similar to that of Ce^{3+} (0.103 nm) and Ce^{4+} (0.092 nm), and in an octahedral coordination environment they all fit well in a common FCC crystal structure. It is obvious that the principal peak positions of the *x*Cu/Ce catalysts first move to higher binding energy with increasing copper amount from 5 to 10 mol.% and then shift to lower BE for 15 mol.%, indicating that the interaction between Cu species and CeO_2 is highest over the 10Cu/Ce sample. Copper reduction is evaluated by determining the intensity of satellite peaks relative to that of main peaks (I_{sat}/I_{pp}). It is well known that the I_{sat}/I_{pp} value of bulk CuO is 0.57, and a lower I_{sat}/I_{pp} value means more Cu^+ species and stronger Cu–Ce interaction. As depicted in Table S2, the I_{sat}/I_{pp} values for the *x*Cu/Ce catalysts are lower than 0.57, confirming the existence of Cu^+ in the Cu-doped CeO_2 samples. In addition, the I_{sat}/I_{pp} value of 10Cu/Ce is lower than those of 5Cu/Ce and 15Cu/Ce, indicating optimized interaction between copper and ceria. The Cu LMM Auger spectra of *x*Cu/Ce catalysts were measured to further verify the presence of Cu^+ species. As shown in Fig. 2C, two peaks at 912.8 and 917.4 eV are detected over the *x*Cu/Ce samples, which can be ascribed to Cu^+ and Cu^{2+} species, respectively. In addition, the peak-splitting results of the Cu LMM Auger spectra show that the Cu^+/Cu^{2+} values of 5Cu/Ce, 10Cu/Ce, and 15Cu/Ce are 0.31, 0.42, and 0.35, respectively. Therefore, the doublet peaks of the Cu LMM spectra give strong evidence to confirm the coexistence of Cu^{2+} and Cu^+ in the catalysts.

To further verify the presence of Cu^+ species in the 10Cu/Ce catalyst, we employed CO as a probing molecule and performed in situ DRIFTS characterization. As shown in Fig. 2D, there are three spectral zones at 30 °C. The absorption IR band located at around 3660 cm^{-1} is ascribed to the stretching band of isolated hydroxyls that comes from monocoordinated and multicoordinated cerium cations [29]. The IR band centered at 2860 cm^{-1} is attributed to formate species, which may be due to the interaction of CO with –OH groups (i.e., CO + −OH ↔ HCOO−). The two bands at 2120 and 2170 cm^{-1} could result from linear CO adsorbed onto Cu^+ and Cu^{2+} sites, respectively. The stable Cu^+–carbonyl species of 10Cu/Ce indicates the presence of Cu^+ species in the catalyst. The third spectral zone below 1800 cm^{-1} corresponds to different types of carbonate species in CeO_2. The intense bands at 1280 and 1630 cm^{-1} are ascribed to bidentate carbonates result from CO reaction with basic OH groups. In addition, the adsorption of CO on basic surface lattice oxygen leads to monodentate (1530, 1430, and 1060 cm^{-1}), bridged (1710 and 1060 cm^{-1}), and bidentate (1530 and 1060 cm^{-1}) carbonates [30], which are formed according to the process $CuO/CeO_2 + CO \rightarrow Cu^+ + CeO_{2-x} + CO_3^{2-}$. Upon CO adsorption at 100 and 150 °C, the peak intensity of Cu^+–carbonyl species decreases and shifts to lower wavenumber. The red shift (Δ6 cm^{-1}) of the Cu^+–CO band suggests strong π-backbonding and enhanced interaction between chemisorbed CO and Cu^+ ions [31]. The results not only demonstrate the existence of Cu^+ species in the 10Cu/Ce sample but also indicate the strong interaction between CuO_x and CeO_2.

Nitrogen adsorption/desorption experiments were conducted to determine the pore structure of the *x*Cu/Ce catalysts. As plotted in Fig. S5A, the four samples all display characteristic type IV isotherms with well-defined type H1 hysteresis loops in relative pressure (P/P_0) ranging from 0.6 to 1.0, suggesting a mesoporous structure with good pore connectivity [32,33]. This is proved by the results of the corresponding pore-size distribution calculated based on the Barrett–Joyner–Halenda (BJH) method. In Fig. S5B, the four samples all have smaller mesopores of ca. 7–9 nm and larger mesopores of 9–11 nm; the unique pore structure is formed by the decomposition of urea ($CO(NH_2)_2 + H_2O = CO_2\uparrow + 2NH_3\uparrow$). The presence of a bimodal porous structure confers excellent mass transport of reactants (and products) to (and from) active sites located inside the framework or interparticulate mesopores, thus facilitating the enhancement of catalytic performance [34]. On the basis of N_2 adsorption–desorption isotherms, the textural parameters were calculated using the Brunauer–Emmett–Teller (BET) and BJH models, and are summarized in Table 1. The BET surface area and pore volume of *x*Cu/Ce catalysts first increase with the increase of Cu content up to 10 mol.% due to the decrease of CeO_2 crystal size with the introduction of copper and PVP, in accord with the XRD results. Further increase of copper content would result in a decrease of pore volume and BET surface area owing to pore blockage caused by the aggregation of excessive copper. The PVP in the catalyst could be removed by hypochlorite treatment, in which hypochlorite reacts with the pyrrolidone ring of PVP, leading to chain scission of PVP molecules (Fig. S6).

As revealed in the SEM images of Fig. 3, all the *x*Cu/Ce catalysts show a rodlike morphology 200–600 nm in length and ca. 30 nm in diameter. The pristine CeO_2 has a short-rod morphology together with a certain number of nanoparticles. With increased copper content, the nanorods of 5Cu/Ce and 10Cu/Ce become longer, while some of the nanorods of 15Cu/Ce become even larger in diameter. The results indicate that the addition of a suitable amount of copper is conducive to the formation of uniform rod morphology. To gain insight into the growth mechanism of the *x*Cu/Ce catalysts, time-dependent experiments were conducted as presented in Fig. S7. In the initial stage, the poorly crystallized CeO_2 nuclei aggregate to form CeO_2 nanoparticles with a mean diameter of 20–40 nm as determined by the minimization of total energy [35]. At a synthesis time of 24 h, rodlike structures evolve from nanoparticles of larger size under base conditions, which are controlled by the addition of $NH_3{\cdot}H_2O$.

To get deeper insight into the microstructure, TEM investigations of the 10Cu/Ce catalyst were performed and the results are presented in Fig. 4. 10Cu/Ce is composed of nanorods 200–

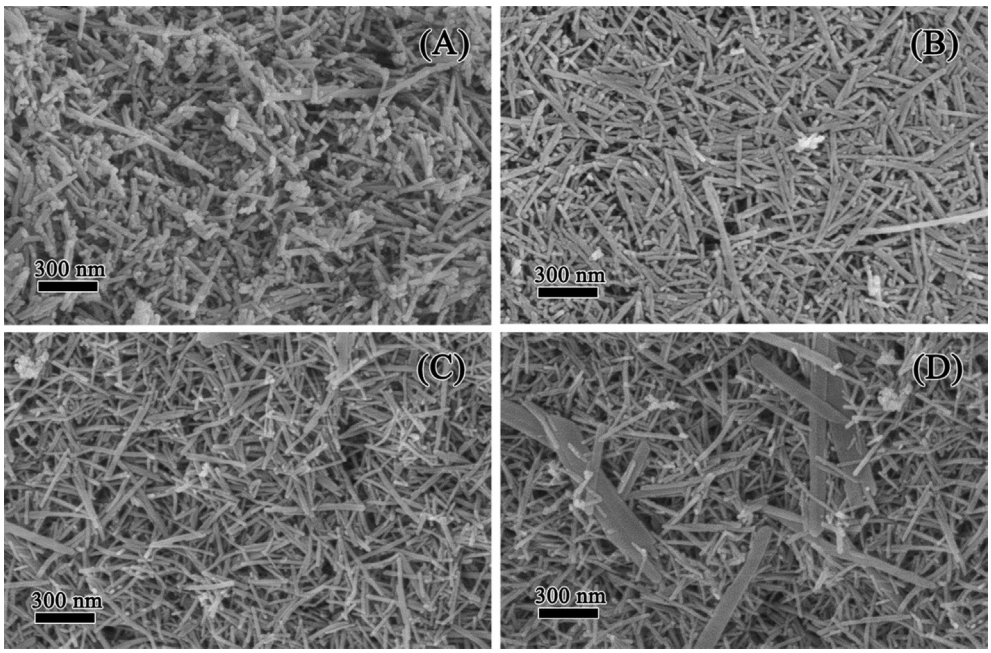

Fig. 3. SEM images of *x*Cu/Ce catalysts: (A) CeO_2, (B) 5Cu/Ce, (C) 10Cu/Ce, and (D) 15Cu/Ce.

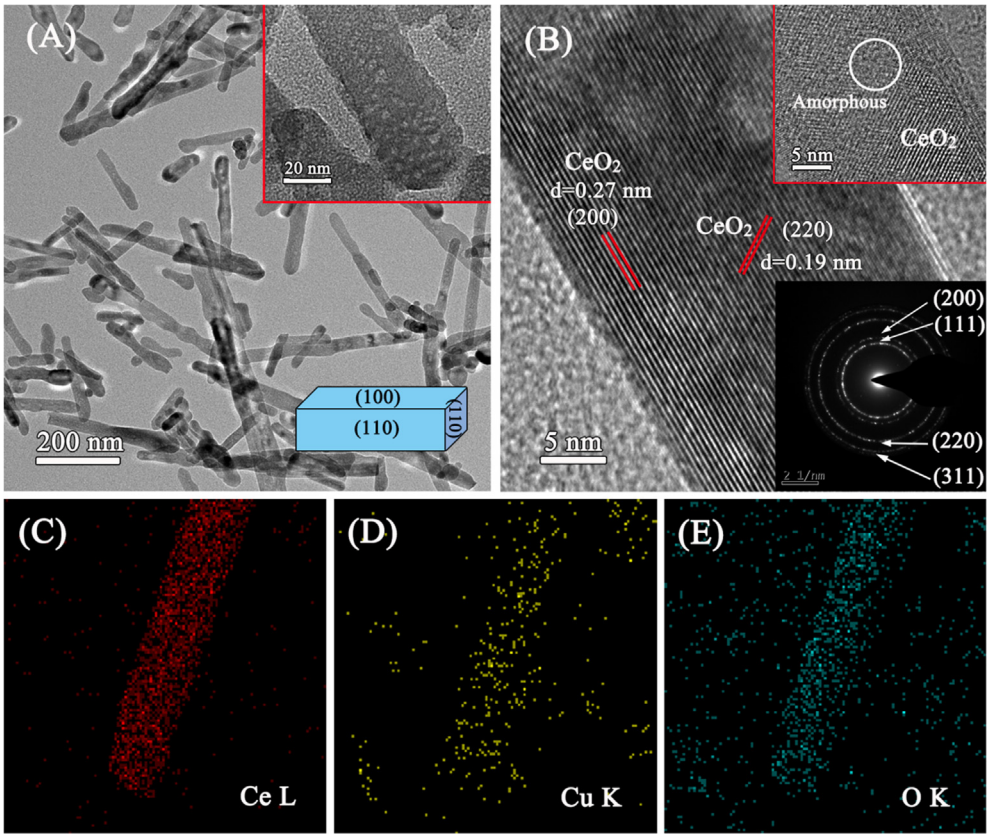

Fig. 4. (A) TEM images, (B) corresponding HRTEM images, SAED pattern (inset) and (C, D, E) STEM-EDX maps of 10Cu/Ce catalyst.

600 nm in length and ca. 30 nm in diameter (Fig. 4A). A magnified TEM image (the inset) gives the evidence of a porous structure that is distributed over the rods with an average pore size of about 7.5 nm (Fig. S8), which is in line with the results of nitrogen adsorption. The observed porous structure, with abundant mesoporous channels, allows efficient mass transfer and guest adsorption [36]. The HRTEM image of Fig. 4B shows that the surface of 10Cu/Ce is covered predominately with (200) and (220) crystallographic planes with interplanar spacings of 0.27 and 0.19 nm as determined by the fast Fourier transform (FFT) algorithm, respec-

tively belonging to the (100) and (110) crystal faces of ceria. Thus, the large number of oxygen vacancies in the 10Cu/Ce catalyst should be attributed to the (100) and (110) planes, acknowledging that the activation energy for the formation of oxygen vacancies on these planes is lower than that on (111) plane [37]. Additionally, the top right inset image of Fig. 4B indicates that the amorphous CuO_x surface without lattice fringes is presented adjacent to the ceria nanorods [38]. The SAED pattern (presented in the lower right inset) corresponding to the (111), (200), (220), and (311) planes confirms the formation of polycrystalline ceria. The elemental mapping analysis derived from EDX spectroscopy (Figs. 4C–E) indicates the good distribution of Cu, Ce, and O throughout the nanorod.

3.2. Catalytic performance

Fig. 5A shows the results of H_2S conversion for the *x*Cu/Ce catalysts. Overall, the H_2S conversion over the *x*Cu/Ce catalysts gradually increases and becomes close to 100% with reaction temperature rising to 250 °C. Apparently, the 10Cu/Ce catalyst shows excellent catalytic performance, offering almost complete H_2S conversion at 220 °C. For comparison, 15Cu/Ce, 5Cu/Ce, and CeO_2 display 100% H_2S conversion at 250 °C while CuO catalyst only exhibits 94.1% H_2S conversion at 250 °C (Fig. S9). In brief, the H_2S conversion of the catalysts displays a decreasing order of 10Cu/Ce > 15Cu/Ce > 5Cu/Ce > CeO_2, in line with the trend of oxygen vacancy concentration and the interaction between copper species and ceria reflected in Raman, EPR, and XPS analyses. The results indicate that the two factors have a strong influence on the activity of *x*Cu/Ce catalysts in H_2S selective oxidation. The sulfur selectivity of *x*Cu/Ce catalysts with respect to reaction temperature is presented in Fig. 5B. It is clear that the sulfur selectivity over 10Cu/Ce is constantly close to 100% in the investigated temperature range. The sulfur selectivity of 15Cu/Ce suffers a decrease when the reaction temperature surpasses 220 °C, whereas that of 5Cu/Ce and CeO_2 decreases at 190 °C, mainly owing to the occurrence of side reactions (i.e., $2H_2S + 3O_2 \rightarrow 2SO_2 + 2H_2O$; $S + O_2 \rightarrow SO_2$) [39]. Overall, 10Cu/Ce is the highest in sulfur selectivity, followed by 15Cu/Ce and 5Cu/Ce, while pure CeO_2 is the lowest. It can be found that the sulfur selectivity of the *x*Cu/Ce catalysts is higher than 90% over the entire temperature range applied for the activity test.

The sulfur yields of *x*Cu/Ce catalysts with respect to temperature are illustrated in Fig. 5C. It is seen that the tendency of sulfur yield is close to that of H_2S conversion due to the high sulfur selectivity. As for the 10Cu/Ce catalyst, the sulfur yield first increases with increasing temperature to 220 °C and remains steady (ca. 100%) at 250 °C. For comparison, the CeO_2 and CuO catalysts exhibit 91% and 66.6% sulfur yield, respectively, under the same conditions. In other words, the 10Cu/Ce catalyst is the highest in sulfur yield among the *x*Cu/Ce samples, and is also higher than the Ce-based catalysts listed in Table S3. According to the above analysis, it is reasonable to conjecture that the catalytic performance of *x*Cu/Ce catalysts for selective H_2S oxidation is dramatically influenced by the doping of copper ions into the CeO_2 lattices. With regard to the major factors that influence catalytic performance, it will be further elaborated below.

In view of the high catalytic performance of 10Cu/Ce, the influence of H_2S/O_2 molar ratio, WHSV, and water vapor on catalytic performance was studied. Fig. 6A displays the influence of H_2S/O_2 molar ratio on catalytic performance of 10Cu/Ce at 220 °C. The H_2S concentration was maintained at 5000 ppm and the H_2S/O_2 molar ratio varied from 1:2 to 3:1. It is clearly found that 95% H_2S conversion and 100% sulfur selectivity can be obtained at H_2S/O_2 = 3; the additional H_2S may be converted into disulfides (H_2S_2, HS_2^-, or S_2^{2-}) and adsorbed on the catalyst [40]. With an

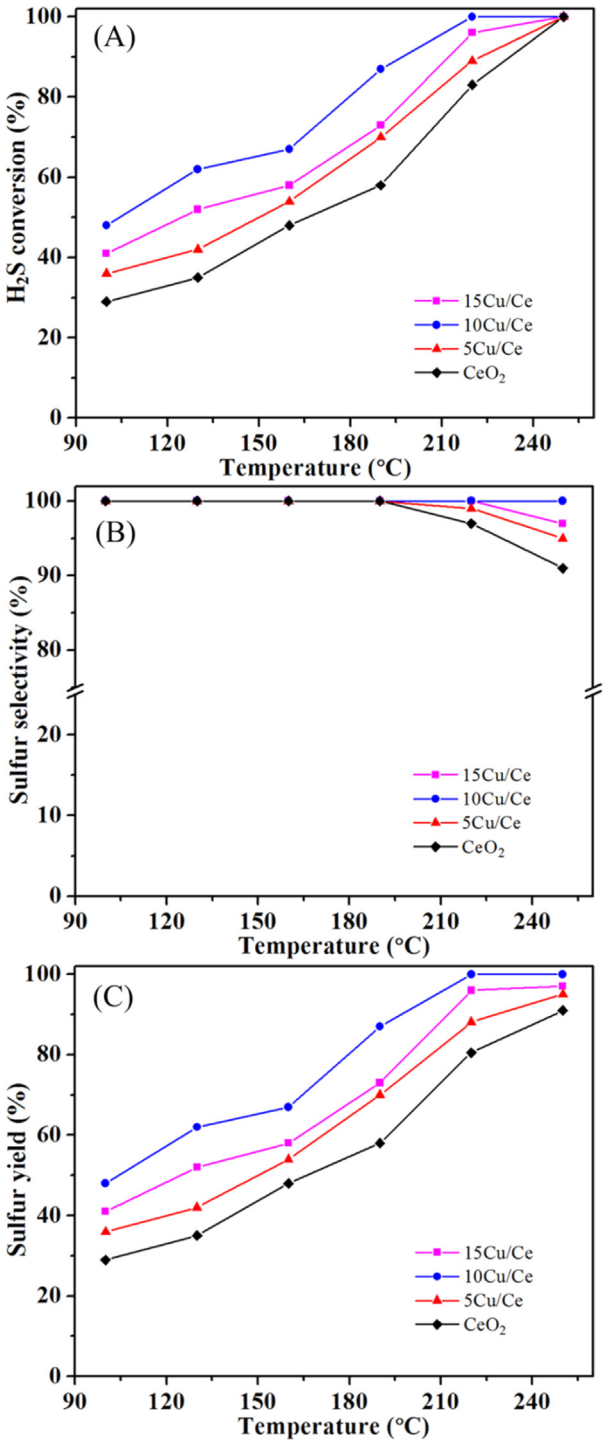

Fig. 5. (A) H_2S conversion, (B) sulfur selectivity, and (C) sulfur yield for H_2S selective oxidation over the CeO_2 and *x*Cu/Ce catalysts.

increase of O_2 concentration, H_2S conversion increases to nearly 100% and sulfur selectivity remains close to 100%. In addition, sulfur selectivity suffers a decrease from 94% to 86% as the H_2S/O_2 molar ratio decreases from 1:1 to 1:2, while H_2S conversion stays at ca. 100%. The 10Cu/Ce catalyst achieves 100% sulfur yield under stoichiometric proportion (H_2S/O_2 = 2), and it then levels off with increasing O_2 concentration. These results indicate that the H_2S/O_2 molar ratio has a significant influence on the catalytic performance of CeO_2-based materials in H_2S selective oxidation. An insufficient oxygen supply would lead to low H_2S conversion, while excessive oxygen could facilitate H_2S deep oxidation [41,42].

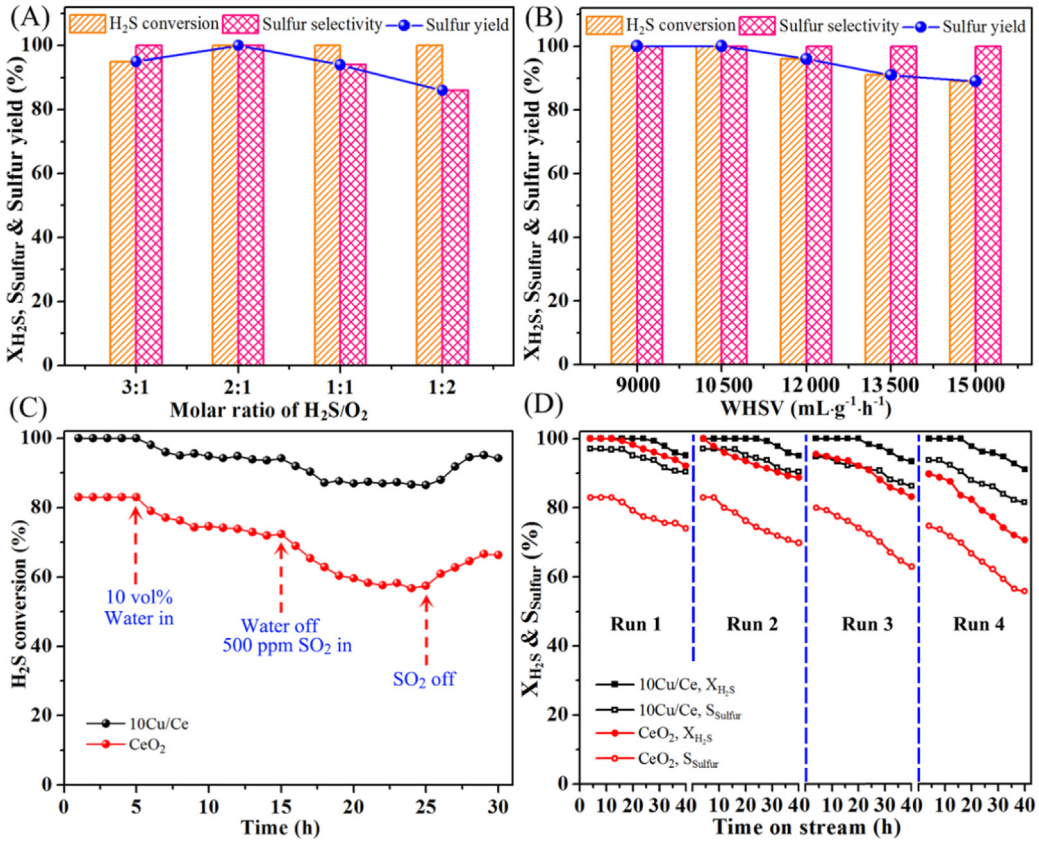

Fig. 6. Effect of (A) H_2S/O_2 molar ratio and (B) WHSV on catalytic performance of the 10Cu/Ce catalyst; (C) 10 vol% H_2O and 500 ppm SO_2 tolerance tests and (D) durability test of the 10Cu/Ce and CeO_2 catalysts at 220 °C (X_{H2S} and S_{Sulfur} represent the H_2S conversion and sulfur selectivity, respectively). Reaction conditions: 0.2 g of catalyst, gas flow rate = 35 mL·min^{-1}, $H_2S/O_2/N_2$ = 0.5/0.25/99.25 (vol.%)).

To understand the influence of WHSV on the catalytic performance of 10Cu/Ce, a series of experiments were conducted with WHSV varied from 9000 to 15 000 mL·g^{-1}·h^{-1}. As depicted in Fig. 6B, nearly 100% H_2S conversion is obtained at WHSV below 10 500 mL·g^{-1}·h^{-1}. Subsequently, it decreases with further increase of WHSV (89% H_2S conversion at 15 000 mL·g^{-1}·h^{-1}). On the other hand, sulfur selectivity remains constant at 100% in a WHSV range of 9000–15 000 mL·g^{-1}·h^{-1}. In spite of sulfur yield suffering a decrease at WHSV of 15 000 mL·g^{-1}·h^{-1}, it is still higher than 90% on account of the high sulfur selectivity.

As can be seen from the above results, 10Cu/Ce shows excellent catalytic activity in the absence of water vapor or SO_2. However, the presence of H_2O(g) and SO_2 in sulfur-containing streams is known to have adverse effects on catalytic activities [43]. Hence, we studied the effect of H_2O and/or SO_2 on H_2S selective oxidation over 10Cu/Ce and CeO_2 at 220 °C. As shown in Fig. S10, the 10Cu/Ce catalyst exhibits sulfur selectivity and H_2S conversion of ca. 100% in the presence of 5 vol% water vapor. When the vapor is 15 vol %, there is a decrease of sulfur yield and H_2S conversion, while sulfur selectivity still remains close to 100%. A further increase of water vapor would result in a decrease of H_2S conversion, sulfur selectivity, and sulfur yield. Then we investigated the effect of adding separately 10 vol% H_2O and 500 ppm SO_2 on catalytic performance vs. time (Fig. 6C). Over 10Cu/Ce, the introduction of 10 vol % H_2O for an on-stream time of 5 h causes rapid decrease of H_2S conversion from 100% to 93%, which remains almost unchanged afterward, while over CeO_2, the decrease is from 83% to 72%. The partial deactivation of the catalyst may be attributed to the competing adsorption of H_2O and H_2S at the same active sites. In addition, the addition of water vapor would give rise to the reverse Claus reaction (i.e., $3S + 2H_2O \leftrightarrow SO_2 + 2H_2S$), leading to a decrease of H_2S conversion and sulfur selectivity. When 500 ppm of SO_2 is subsequently introduced after the cessation of H_2O supply, H_2S conversion over 10Cu/Ce decreases from 93% to 86%, which is due to Cu and Ce species tending to react with SO_2 to form sulfates, resulting in inactivation and poisoning of catalysts. With the cessation of SO_2 supply, there is a recovery of H_2S conversion to ca. 94%. In contrast, the CeO_2 catalyst exhibits lower performance in terms of SO_2 resistance, and H_2S conversion decreases to ca. 55% upon similar treatment. According to the above results, it is reasonable to deduce that the 10Cu/Ce catalyst can tolerate water vapor and SO_2 to a certain extent, indicating its potential for desulfurization in industries.

Durability of catalysts is a key criterion for industrial applications, and the stability result for the 10Cu/Ce catalyst is presented in Fig. 6D. In the case of undoped CeO_2, H_2S conversion is constantly ca. 83% in the initial 12 h and then gradually decreases. The sulfur selectivity over CeO_2 starts to decrease after 8 h. The poor stability of undoped CeO_2 may be due to sulfur deposition and the formation of sulfate in a long-term reaction. As for the 10Cu/Ce catalyst, the H_2S conversion and sulfur selectivity remain ca. 100% within reaction periods of 26 h and 16 h, respectively, after which a gradual decrease is observed. To explore the cyclic stability of the catalyst, the spent catalyst was regenerated by raising the catalyst temperature to 450 °C under a stream of N_2 (60 mL/min) for 120 min to eliminate the formed sulfur. After three regenerations, the 10Cu/Ce catalyst shows a H_2S conversion and a sulfur selectivity of 91% and 82%, while pure CeO_2 shows 71% and 56%, respectively. The higher stability of 10Cu/Ce is attributed to the preferential interaction of SO_2 with Cu, which effectively protects the adjacent cerium species from SO_2 poisoning [44]. In addition, the large numbers of oxygen vacancies facilitate efficient O_2

activation, hindering the formation of byproducts as a consequence, and the porous structure confers excellent mass transport that is beneficial for long-time durability [45]. The recovered sulfur (Fig. S11) and that in the used catalyst calculated on the basis of mass balance have a gross value of ca. 97%, which is close to the sulfur yield.

3.3. Kinetic analysis

The H_2S conversion rates were kept under 20% to eliminate the effect of internal/external diffusion. The following elementary steps are proposed to describe the reaction mechanism for H_2S oxidation:

$$H_2S + 2^* \rightleftarrows H^* + {}^*SH \quad (R1)$$

$$O_2 + 2^* \rightleftarrows 2O^* \quad (R2)$$

$$O^* + {}^*SH \rightarrow {}^*OH + S + {}^* \quad (R3)$$

$${}^*OH + H^* \rightleftarrows H_2O + 2^* \quad (R4)$$

$$H_2S + (1/2)O_2 = S + H_2O \text{ (overall reaction)}$$

Here, an asterisk (*) stands for an active site and S is the formed sulfur. The symbols in the above equations represent equilibrium (⇄) and rate-determining (→) steps, respectively [46]. This set of elementary steps includes (1) adsorption and dissociation of H_2S and O_2 on the catalyst surface (equilibrium reactions R(1) and R (2)); (2) reaction between SH and O, which is assumed to be the rate-determining step (reaction R(3)); (3) formation of H_2O (reaction R(4)).

The equilibrium constants for steps R1 and R2 are given by the following expressions:

$$K_1 = \frac{[H*][*SH]}{[H_2S][*]^2} \quad (7)$$

$$K_2 = \frac{[O*]^2}{[O_2][*]^2} \quad (8)$$

The concentration of the total active sites "[L]" is given by

$$[L] = [*] + [S] + [H*] + [*SH] + [O*] + [OH*] \approx [*] + [S]. \quad (9)$$

Here is the simplification due to the *mari* concept [46]. Substituting equation (9) in Eqs. (7) and (8),

$$[*SH] = \frac{K_1[H_2S][*]^2}{[H*]} = \frac{K_1[H_2S]([L]-[S])^2}{[H*]}, \quad (10)$$

$$[O*] = {K_2}^{0.5}[O_2]^{0.5}[*] = {K_2}^{0.5}[O_2]^{0.5}([L]-[S]). \quad (11)$$

The reaction rate for step R3 is expressed as follows:

$$r_s = k_1[O*][*HS]. \quad (12)$$

Substituting Eqs. (10) and (11) into Eq. (12), the rate expression becomes

$$r_s = k_1[O*][*HS]$$

$$= \frac{k_1K_1{K_2}^{0.5}[H_2S][O_2]^{0.5}([L]-[S])^3}{[H*]}$$

$$= \frac{k_1K_1{K_2}^{0.5}[H_2S][O_2]^{0.5}[L]^3}{[H*]}\left(1-\frac{[S]}{[L]}\right)^3 \quad (13)$$

Here, "1 – [S]/[L]" reflects the effect of produced sulfur on the H_2S oxidation process. When [S] = [L], it means that all the active sites have been covered with sulfur, and the reaction rate is zero. Therefore, "1 – [S]/[L]" can be defined as a function of sulfur deposition, which could be expressed by the empirical correlation of the power function:

$$\Phi_s = \left(1-\frac{[S]}{[L]}\right)^3 = (1-\alpha W_s)^n. \quad (14)$$

Here, α is a parameter related to [L] and W_s is the mass of the formed sulfur:

$$\alpha = \frac{k'}{[L]^3}. \quad (15)$$

Substituting Eqs. (14) and (15) into Eq. (13), the rate of sulfur formation can be expressed as

$$r_s = \frac{dW_s}{dt} = \frac{k_1K_1{K_2}^{0.5}(k'/\alpha)[H_2S][O_2]^{0.5}}{[H*]}(1-\alpha W_s)^n. \quad (16)$$

On simplification,

$$\frac{dW_s}{dt} = \left(\frac{k}{\alpha}\right)[H_2S][O_2]^{0.5}(1-\alpha W_s)^n. \quad (17)$$

Here,

$$k = \frac{k_1k'K_1{K_2}^{0.5}}{[H*]}. \quad (18)$$

k is the reaction rate constant, which is a function of temperature and the surface properties of the catalyst.

On integration, Eq. (17) is expressed as follows:

$$W_s = \begin{cases} [1-exp(-\alpha r_{s0}t)]/\alpha \ (n=1) \\ \frac{1}{\alpha}\{1-1/[1+(n-1)\alpha r_{s0}t]^{[1/(n-1)]}\} \ (n\neq 1) \end{cases}, \quad (19)$$

$$r_{s0} = \left(\frac{k}{\alpha}\right)[H_2S][O_2]^{0.5}. \quad (20)$$

r_{s0} is defined as the initial desulfurization rate at $W_s = 0$. The parameter n can be determined by fitting the experimental data of W_s and t with the least-squares method. The calculated results show that a good correlation coefficient was obtained for most experimental data when $n = 2$. Thus, Eq. (19) can be written as

$$\frac{1}{W_s} = \alpha + \frac{1}{r_{s0}}\cdot\frac{1}{t}. \quad (21)$$

To determine the kinetic parameter, a plot is made for $1/W_s$ against the reciprocal of time $1/t$ at five temperatures. As shown in Fig. 7A, the straight lines indicate that the model fits well with the experimental data. The linear fitting degree increases with the rise of temperature, which suggests that the hypothesis is correct. That is, the reaction between SH and O is the rate-controlling step [47,48].

We obtained α and r_{s0} from the intercepts and slopes of the straight lines in Fig. 7A, and then the rate constant k could be calculated according to their relationship with $[H_2S]$ and $[O_2]$; the results are listed in Table S4. As displayed in Fig. 7B, there is a good linear relationship between the kinetic constant k and $1/T$, indicating that the kinetic constant satisfies the Arrhenius equation. The activation energy (E_a) is calculated on the basis of the Arrhenius formula [49]:

$$k = A\exp(-E_a/RT) \quad (22)$$

Here, A is the pre-exponential factor, and R and T are the gas constant (R = 8.314 J/(mol·K)) and the reaction temperature (K), respectively. Fig. S12 shows the relationship between α and the

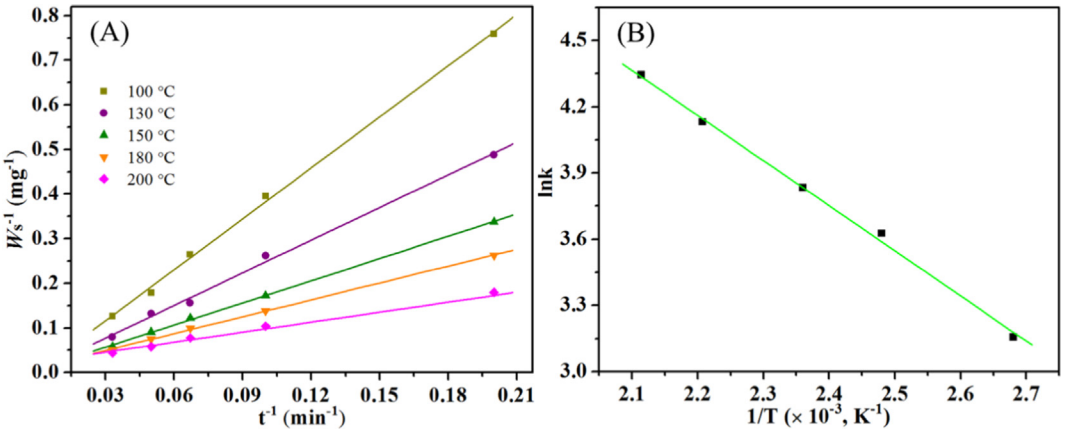

Fig. 7. (A) Plots of $1/W_s$ against $1/t$ and (B) plots of ln k against $1/T$ for H_2S oxidation over the 10Cu/Ce catalyst.

corresponding reaction temperature. It can be seen that there is an approximately linear relationship between the two within the experimental temperature range:

$$\alpha = -0.05 + 1.42 \times 10^{-4}T \quad (23)$$

Based on the above analysis, the reaction rate expression for H_2S oxidation is established as follows:

$$r_s = (k/\alpha)[H_2S][O_2]^{0.5}(1 - \alpha W_s)^2 \quad (24)$$

The kinetic parameters in the formula are:

$$k = 5875\exp(-2057.9/T), \quad (25)$$

$$\alpha = -0.05 + 1.42 \times 10^{-4}T \quad (26)$$

The TOF values and reaction rates of H_2S selective oxidation over xCu/Ce were also calculated and are presented in Table 2. It can be found that the Cu dispersion in the catalysts increases with increasing Cu content up to 10 mol.% due to larger BET surface area promoting the dispersion of copper ions [50]. The TOFs and reaction rates of H_2S conversion are strongly dependent on the amount of Cu doping. It can be found that the TOF value and reaction rate of the 5Cu/Ce sample are higher than those of CeO_2 due to the higher oxygen vacancy concentration and good dispersion of copper species on 5Cu/Ce, as supported by the results of Raman and XRD analyses. With increasing content of Cu to 10 mol.%, the TOF value and reaction rate become higher because of the enriched active copper sites and improved Cu dispersion (Table 2). However, there is a slight decrease of TOF value and reaction rate in the case of 15Cu/Ce, which could be ascribed to the existence of bulk CuO (Fig. 1A). The above results demonstrate that the doping of copper into the CeO_2 lattice improves the reaction rate, resulting in enhanced H_2S conversion.

3.4. Catalytic mechanisms

3.4.1. Catalyst basicity, reducibility, and oxygen species

The basic properties of a catalyst determine its role in the selective oxidation of H_2S. CO_2-TPD-MS experiments were performed to evaluate the surface basicity of the xCu/Ce catalysts. As shown in Fig. 8A, the CO_2-TPD-MS profiles could be divided into three desorption regions with peaks centered at 50–200, 200–460, and 460–660 °C. The three peaks are related to bicarbonate species of CO_2 adsorption onto −OH groups of weak basicity, bidentate carbonates of CO_2 adsorption onto metal–O pairs of medium basic sites, and unidentate carbonates of CO_2 adsorption onto O^{2-} species of strong basicity [51], respectively. In addition, the numbers of basic sites derived from the CO_2-TPD-MS data (Table S5) show that the values increase with the copper content increasing to 10 mol.% and then decrease with further increase of Cu content to 15 mol.%. The enhancement of basicity with the introduction of Cu could be elucidated as follows: the CO_2 molecule is a weak electron donor and a strong electron acceptor. Besides, the electronic shell structure of Cu is $3d^{10}4s^1$ with the d orbits fully occupied by electrons, while that of Ce is $5d^16s^2$, which possesses a large number of unoccupied d orbits. As for the xCu/Ce catalysts, the d electrons of copper species would move to the d orbits of ceria through a Ce^{3+}-□-Cu^+ structure [52]. Thus, compared with bare CeO_2, the xCu/Ce catalysts have greater ability for CO_2 adsorption onto the basic sites. The presence of strong basic sites on 10Cu/Ce is attributed to the large number of oxygen vacancies. Hence the basicity of 10Cu/Ce is higher than that of the other xCu/Ce catalysts. The results demonstrate that the basicity of ceria can be enhanced by the introduction of Cu species, which is conducive to the adsorption of H_2S, leading to improved catalytic activity.

In addition to basic properties, the redox chemistry of ceria also has an effect on catalytic activity. It can be adjusted by controlling the extent of interaction between the metal and ceria [53]. The

Table 2
Kinetics results of the CeO_2 and xCu/Ce catalysts.

Catalysts	Dispersion (%)[a]	Reaction rate ($\times 10^{-7}$ mol·g$_{cat.}^{-1}$·s^{-1})	TOF$_{Cu}$ ($\times 10^{-3}$ s^{-1})[b]	TOF$_{Ce}$ (s^{-1})[c]
CeO_2	–	2.95	–	0.54
5Cu/Ce	10.5	3.36	8.06	0.66
10Cu/Ce	13.5	5.81	9.05	0.94
15Cu/Ce	8.60	4.63	8.42	0.82

[a] Cu dispersion estimated on the basis of N_2O chemisorption.
[b] TOF value calculated based on CuO.
[c] TOF value calculated based on CeO_2.

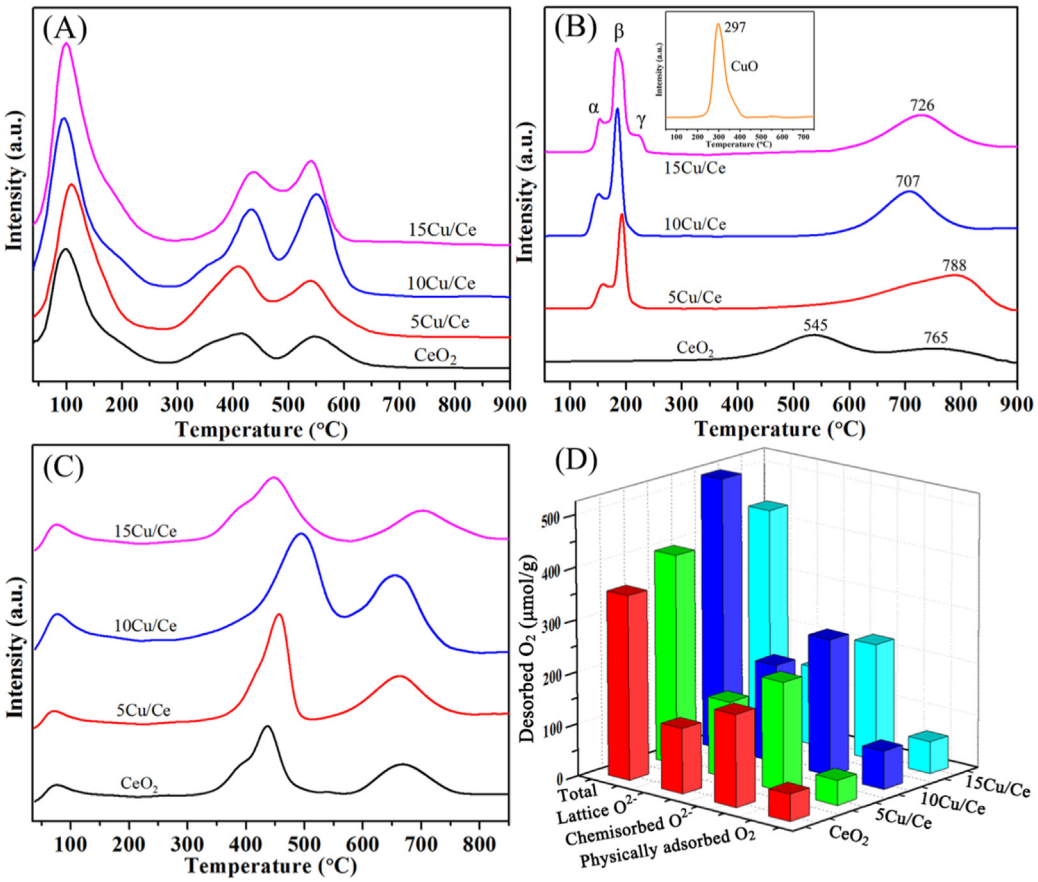

Fig. 8. (A) CO_2-TPD-MS, (B) H_2-TPR, (C) O_2-TPD-MS profiles, and (D) the amount of desorbed O_2 calculated from the TPD profiles of CeO_2 and *x*Cu/Ce catalysts.

H_2-TPR profiles of *x*Cu/Ce catalysts are presented in Fig. 8B, and Table S6 summarizes the reduction temperature and hydrogen consumption related to the reduction of Cu species and surface ceria oxygen. As shown in the inset, pure CuO (synthesized through the ethanol thermal process) shows a single reduction peak at 297 °C ascribed to the reduction of CuO. For the undoped CeO_2 sample, the peaks at 545 and 765 °C correspond to the reduction of coordinately unsaturated capping oxygen and bulk ceria [54], respectively. For the 5Cu/Ce catalyst, there are two reduction peaks at 159 °C (peak α) and 192 °C (peak β). Peak α is the reduction of highly dispersed copper oxide species that have strong interaction with ceria, and peak β is attributed to the reduction of a strongly bound Ce-[O_x]-Cu structure. With the Cu content increasing from 5 to 10 mol.%, both peaks α and β of the 5Cu/Ce catalyst show an increase of intensity and a shift to lower temperature, indicating strong synergism between Cu and CeO_2, namely, weakening of Ce–O bonds by Cu doping and concomitant formation of Cu–O–Ce bonds. This would result in easier reduction of both CuO and CeO_2, as well as enhanced mobility of the surface oxygen species of CeO_2. As for the 15Cu/Ce catalyst, the α and β peak intensity increase slightly and there is a shift to relatively higher reduction temperature in comparison with those of the 10Cu/Ce catalyst. In addition, a new peak (peak γ) at 227 °C can be observed over the 15Cu/Ce catalyst. The peak γ should be due to the reduction of bulk CuO and Cu^+. This is because the Cu^+ species exists stably in the oxygen vacancies and its reduction temperature is higher than that of copper oxide species interacting with ceria, but close to that of bulk CuO [55]. The existence of bulk CuO has been proved in the above XRD analysis. The quantitative results based on the peaks of H_2 consumption (Table S6) show that (i) there is enhanced reducibility of *x*Cu/Ce in comparison with CeO_2 and (ii) the total hydrogen consumption based on peaks α and β is in the order 10Cu/Ce > 15Cu/Ce > 5Cu/Ce, which is in agreement with the result of catalytic activity for H_2S selective oxidation. These results could be interpreted in terms of copper–ceria interaction, which in turn promotes the Ce^{4+}/Ce^{3+} redox ability as well as the generation of active oxygen species, thus enhancing the catalytic activity of the *x*Cu/Ce catalyst for selective oxidation of H_2S. The excellent reducibility of the *x*Cu/Ce catalysts might be attributed to (i) electronic metal–support interactions (EMSI) between ceria and copper nanoparticles and (ii) hydrogen spillover from copper sites to CeO_2 support. These results confirm the valence variation as characterized by the Cu XPS spectra, evidencing the close relation between electronic and redox properties established through metal–support interactions.

An O_2-TPD-MS experiment was conducted on *x*Cu/Ce catalysts to investigate the nature of surface oxygen species involved in H_2S selective oxidation. As presented in Fig. 8C, three prominent desorption peaks at ca. 80, 430, and 660 °C are detected over the samples, which are assigned to the desorption of physically adsorbed O_2, chemically adsorbed O_2^- (ad), and lattice O^{2-} (latt) [56], respectively. The surface oxygen species might be released according to the equations $Cu^+–V_{\ddot{o}}–Ce^{3+} + O_2 \leftrightarrow Cu^+–O_2^-–Ce^{4+}$, $Cu^+–O_2^-–Ce^{4+} + O_2 \leftrightarrow Cu^{2+}–2O_2^-–Ce^{4+}$, and the bulk lattice oxygen induced by the variation of $Cu^{2+} \rightarrow Cu^+$ and $Ce^{4+} \rightarrow Ce^{3+}$. It is noticeable that the desorption peak intensity of *x*Cu/Ce increases with the increase of Cu content, which is in accordance with the O1*s* spectra of XPS analysis. For the *x*Cu/Ce catalysts, the desorption peak of lattice oxygen shifts to lower temperature and becomes slightly stronger with copper content increasing from 0 to 10 mol.%, indicating that the mobility of O^{2-} (latt) is improved by copper doping. Furthermore, the amount of available oxygen

was quantified and is shown in Table S7 and Fig. 8D. It can be observed that the 10Cu/Ce catalyst possesses the largest amount of available oxygen, which suggests that copper doping would remarkably enhance the amount of oxygen that can be desorbed. However, the amount of desorbed oxygen species of 15Cu/Ce is less than that of 10Cu/Ce, which may be due to the enrichment of surface CuO limiting the activation and desorption of surface oxygen. The results of XPS, Raman, and EPR analyses have proven the existence of oxygen vacancies in the *x*Cu/Ce catalysts. Many studies have demonstrated that oxygen vacancies are adsorption centers for gaseous O_2 [57]. For the present study, the oxygen vacancies could act as bridges for the delivery of oxygen from CeO_2 to Cu species. Gaseous O_2 adsorbed onto the oxygen vacancies of *x*Cu/Ce can be activated and transformed to O^{2-} (ad), which improves the mobility of oxygen and consequently promotes catalytic activity for H_2S oxidation.

3.4.2. Reaction pathways

Previous studies have reported several pathways for H_2S adsorption on a catalyst [58]: (i) H_2S adsorbs onto a vacant site, and the dissociative product S^{2-} is incorporated into the lattice of the catalyst; (ii) it adsorbs onto the catalyst surface with the generation of –OH and HS^-; (iii) it reacts with a –OH group to form H_2O and HS^-. To find the adsorption path and reaction intermediates in H_2S selective oxidation, we carried out an in situ DRIFTS study of H_2S (5000 ppm) and O_2 (2500 ppm) adsorption on 10Cu/Ce catalyst at different temperatures. As presented in Fig. 9, there are a couple of adsorption peaks in the DRIFTS spectra after H_2S adsorption at 100 °C. The bands at 2581 cm^{-1} and 1305–1480 cm^{-1} are assigned to the stretching and bending modes of HS^-, respectively. The band at around 3650 cm^{-1} is associated with the OH-stretching mode derived from hydrogen bonding of oxygen atoms of CeO_2 to H atoms of H_2S. The band at 1615 cm^{-1} is ascribed to the v_2 bending mode of water generated in the reaction $H_2S + [O] \rightarrow S + H_2O$ ([O] corresponds to an adsorbed oxygen). At 130–160 °C, the band intensity of the H_2S bending mode increases and that of the stretching mode decreases due to enhancement of H_2S adsorption and reaction of a certain number of H_2S molecules. In addition, a new band is detected at 1728 cm^{-1}, which is assignable to coordinated water generated as a result of H_2S oxidation onto the 10Cu/Ce surface. At 190 °C, new bands at 828–1140 cm^{-1} are observed, which are ascribed to the formation of sulfate. Upon reaction at 220 and 250 °C, the H_2S and H_2O bands almost disappear, whereas the bands of sulfate intensify. Thus, it could be deduced that H_2S adsorbs onto the surface of 10Cu/Ce via route (ii), and these results manifest the vital role of adsorbed oxygen in the reaction.

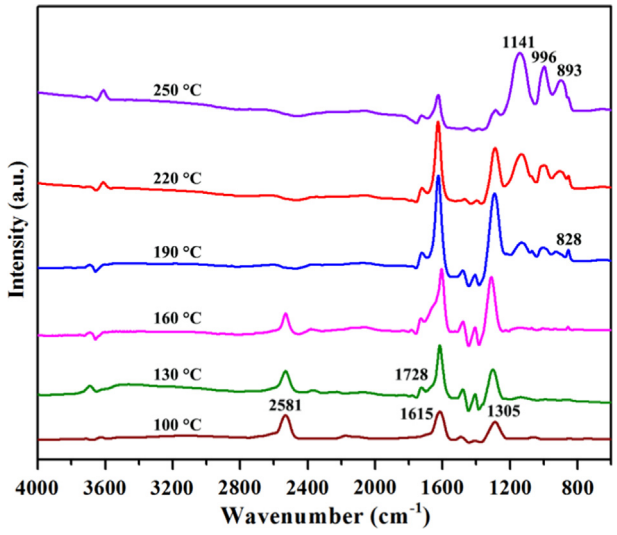

Fig. 9. In situ DRIFTS spectra of H_2S and O_2 co-adsorption on 10Cu/Ce recorded at different temperatures.

3.4.3. Catalyst stability

It is found that the catalytic activity of *x*Cu/Ce suffers a decline after a long reaction time. The XPS spectra of the fresh and used 10Cu/Ce catalyst (after reaction of 40 h) were recorded. The results are shown in Fig. 10 and S13, and the amounts of O_{ad}, Ce^{3+}, and Cu^+ are compiled in Table S2. The Ce3*d* and Cu2*p* results show that there is an increase in the $Cu^+/(Cu^+ + Cu^{2+})$ molar ratio for the used catalyst, accompanied by a slight rise of the $Ce^{3+}/(Ce^{3+} + Ce^{4+})$ molar ratio, providing proofs of the participation of redox cycles. Compared with fresh 10Cu/Ce, used 10Cu/Ce exhibits a positive deviation of 0.5 eV in Cu2$p_{3/2}$ binding energy (BE), while the Ce3*d* BE remains unchanged. It is deduced that the SO_4^{2-} produced in SO_2 oxidation can bond to the copper species, and its high electronegativity results in the decline of electron cloud density around the copper ions and hence the BE increase of the Cu2$p_{3/2}$ peak [59]. As for the O1*s* spectra, the peak intensity of O_{latt} declines after the reaction, while O_{ad} on the catalyst increases compared with that on the fresh one, which is due to the replenishment of reactive oxygen through the adsorption of gaseous O_2 onto surface oxygen vacancies, continuously providing oxygen species for H_2S selective oxidation. In conclusion, the concentration variations of Cu, O, and Ce species reveal that the *x*Cu/Ce materials catalyze H_2S selective oxidation with the participation of Cu^{2+}/Cu^+, Ce^{4+}/Ce^{3+}, and O_{latt}/O_{ad} cycles.

As reported, the decline of catalytic activity after the oxidative desulfurization reaction is mainly due to the formation of sulfate and deposition of S, which has been confirmed by XPS and XRD analyses of the used catalyst. The spectrum of the fresh catalyst presented in Fig. 10C shows no S2*p* signal, whereas the used catalyst shows two peaks at 168.2 eV and 163.5 eV ascribable to sulfate and S [60], respectively. The generation of sulfate can disrupt the Cu^{2+}/Cu^+ and Ce^{3+}/Ce^{4+} redox cycles, and with the retardation of the Cu^+-to-Cu^{2+} and Ce^{3+}-to-Ce^{4+} processes, there is a decline of catalytic activity toward H_2S selective oxidation. The XRD pattern of the used 10Cu/Ce catalyst shows a new peak at $2\theta = 22.6°$ ascribable to sulfur (Fig. 10D), corroborating the deposition of S during the reaction. Meanwhile, the SEM mapping results verify the homogeneous distribution of Ce, Cu, O, and S at a nanometer scale, proving the presence of sulfur on the used 10Cu/Ce catalyst (Fig. S14). In addition, compared with the fresh catalyst, the used one shows a slight decline in specific surface area (from 97.8 to 78.5 $m^2\ g^{-1}$) and pore volume (from 0.56 to 0.51 $cm^3\ g^{-1}$) because of pore blockage by sulfur and sulfate presence, which could cause a decrease of catalytic activity [61]. The boiling point of sulfur is about 450 °C; thus the used catalysts could be regenerated by calcination at 450 °C to remove the deposits of sulfur in the catalyst.

3.5. Density functional theory calculations

3.5.1. Generation of oxygen vacancies

The DFT calculations were employed to verify the effect of copper doping on CeO_2 in terms of the increase of oxygen vacancies. Figs. S15 and S16 present the optimized geometries of an oxygen vacancy on the (110) and (100) surfaces of pristine and Cu-doped CeO_2, respectively. The formation energy of the oxygen vacancy (E_v) was computed based on the equation $E_v = E_{Ce1\text{-}xMxO2\text{-}\delta} + 1/2E_{O2} - E_{Ce1\text{-}xMxO2}$, where $E_{Ce1\text{-}xMxO2\text{-}\delta}$ and $E_{Ce1\text{-}xMxO2}$ represent the energy of pristine/Cu-doped CeO_2 surfaces with or without an oxygen vacancy, and E_{O2} is the energy of a free O_2 molecule. The calculated E_v values over the (110) surface of the pristine and Cu-doped CeO_2

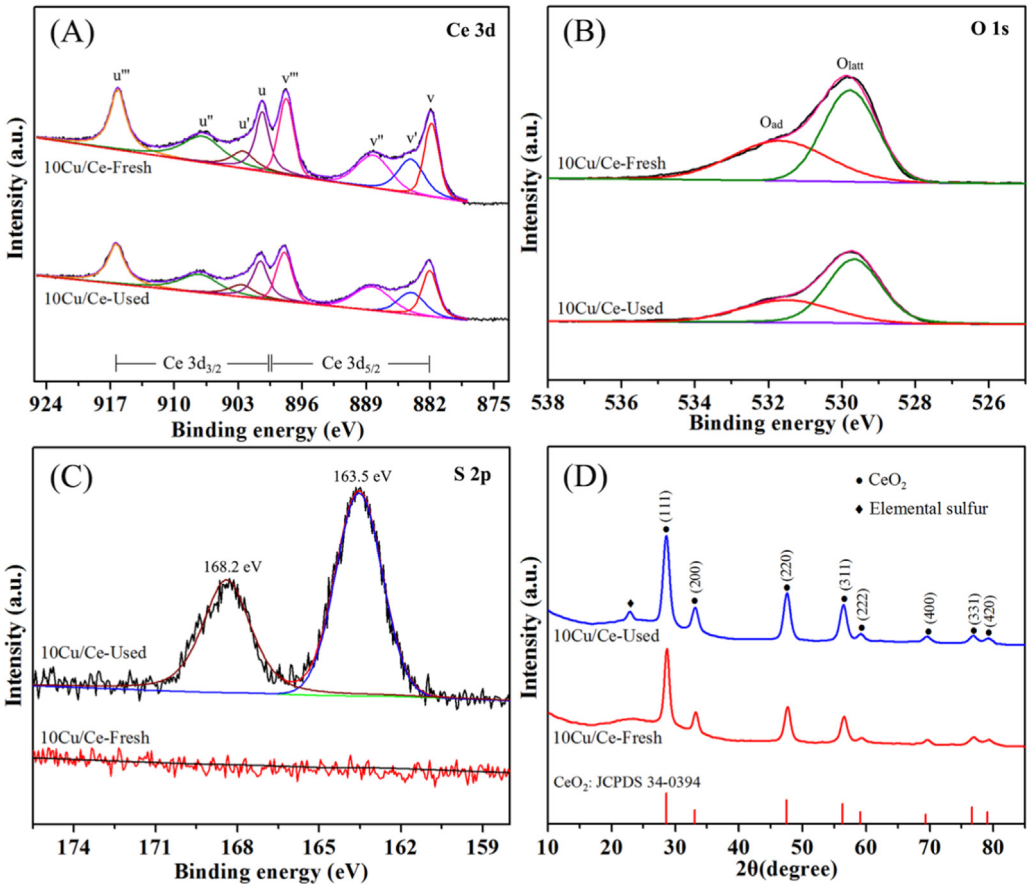

Fig. 10. (A) Ce3*d*, (B) O1*s*, and (C) S2*p* XPS spectra and (D) XRD patterns of fresh and used 10Cu/Ce catalyst.

are 1.93 and −0.69 eV, respectively. In addition, the E_v values over the (100) surface of the pure and Cu-doped CeO_2 are 2.01 and −0.58 eV, respectively. The decline of oxygen vacancy formation energy upon copper doping indicates that the formation of oxygen vacancies is promoted on the surface of Cu-doped CeO_2, which is consistent with the experimental results and reported DFT works [62]. The stable configuration of O_2 adsorption on an oxygen vacancy is shown in Fig. S17. The O_2 molecule lies on the site of the oxygen vacancy and bonds with the cerium atom, having Ce–O bond distances of 2.416 and 2.463 Å. The calculated O_2 adsorption energy is −0.3 eV, suggesting that O_2 adsorption is thermodynamically favorable [63]. In addition, the O–O bond distance (1.331 Å) is larger than that of free O_2 (1.233 Å), indicating O_2 chemisorption. Thus, the activation of the O_2 molecule occurs more readily on the defect CeO_2 surface.

3.5.2. Selective oxidation of H_2S

To better understand the mechanism of H_2S selective oxidation on a Cu-doped CeO_2 (110) surface, we studied the pathway by means of transition state (TS) search. Figs. 11 and S18 present the relative energy profile and corresponding structures in the mechanism for H_2S selective oxidation, respectively. First, the H_2S molecule is adsorbed at an oxygen vacancy and the H_2S adsorption energy is −0.82 eV (LM1), indicating that the presence of an oxygen vacancy facilitates H_2S adsorption [64]. Then, an O_2 molecule adsorbs onto the catalyst surface (LM2) and the calculated O_2 adsorption energy is −0.31 eV. The dissociation of H_2S ($H_2S \rightarrow HS + H$) on the Cu-doped CeO_2 (110) surface (LM3) is exothermic, and a transition state TS1 is searched for with an energy barrier of 0.72 eV. Then, HS reacts with adsorbed O_2 to form

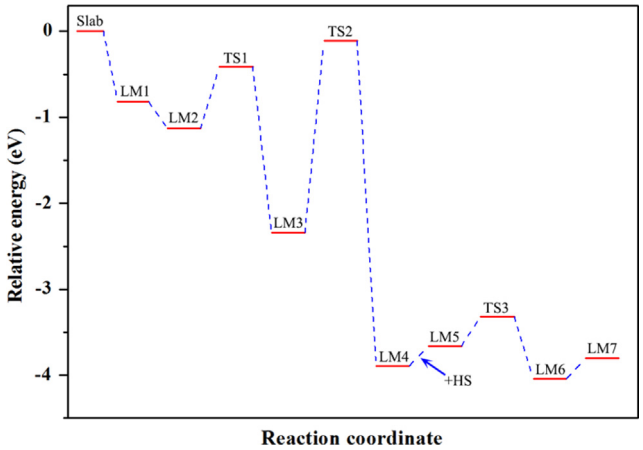

Fig. 11. Schematic of relative energy profile for H_2S oxidation on reduced Cu-doped CeO_2 (110) surface.

sulfur, OH, and O* by overcoming an energy barrier of 2.23 eV (LM4). The formed O* reacts directly with an additional HS (LM5) to form S and OH (LM6), through a small energy barrier of 0.34 eV (TS3). Finally, the OH can react with the H atom dissociated from H_2S to produce H_2O, followed by barrierless H_2O desorption (LM7). The desorption energy of sulfur on a reduced Cu-doped CeO_2 (110) surface was calculated by the equation $\Delta E = E_{Ov\text{-}2H} + E(\frac{S8}{8}) - E_{Ov\text{-}2H\text{-}S}$, and the calculated ΔE value is 0.34 eV, which indicates that it is easy for the formed sulfur to desorb from the Cu-doped CeO_2 (110) surface. Overall, the results indicate that

the reaction between HS^- and $O_{2(ads)}$ is the rate-controlling step, with an energy barrier of 2.23 eV (TS2).

3.5.3. Charge density distribution and SO_2 adsorption

The above XPS results demonstrated that the valence states of Cu and Ce species have changed upon copper doping, which indicates electron transfer from Cu to Ce. To further study the effect of Cu dopant and confirm the occurrence of electron transfer, the differential charge densities of Cu-doped CeO_2 were estimated via spin-polarized period DFT calculations using the formula $\rho_{diff} = \rho_{Ce1\text{-}xCuxO2\text{-}\delta} - (\rho_{Ce1\text{-}xO2\text{-}\delta} + \rho_{Cu})$. As presented in Figs. 12A and B, there is electron transfer from the Cu atom to the Ce atom. Therefore, the valence state of Ce species near the doping site decreases due to the obtained electrons, that is, $Ce^{4+} + Cu^+ \rightleftharpoons Ce^{3+} + Cu^{2+}$, in accordance with XPS analysis. Additionally, the gradual decline of catalytic activity over ceria in selective H_2S oxidation is due to the reaction of SO_2 and O_2 with Ce^{4+} to form sulfate: $2CeO_2 + 3SO_2 + O_2 = Ce_2(SO_4)_3$ [65]. Nonetheless, the doping of Cu species to ceria results in *x*Cu/Ce catalysts with improved sulfur resistance, which could be due to the $Ce^{4+} + Cu^+ \rightleftharpoons Ce^{3+} + Cu^{2+}$ cycles [66].

Meanwhile, we studied the adsorption of SO_2 onto a reduced (110) surface by DFT calculations. Fig. S19 shows SO_2 adsorption on various sites of pure ceria (110) surface. The results show that the most stable configuration is V_1–SO_2(a) with an adsorption energy of −2.95 eV. This model could be described as follows: During SO_2 adsorption, an oxygen atom of SO_2 positioned above an oxygen vacancy forms a Ce–O bond with the Ce atom at the defect. The other O of SO_2 forms another Ce–O bond with the Ce atom derived from the breaking of a Ce–O bond adjacent to the O vacancy, and the O atom released from the broken Ce–O bond attaches to the S of SO_2 to form an S–O bond. In the case of SO_2 adsorption onto Cu-doped $CeO_{2\text{-}x}$, V_2–SO_2(a) is the most stable model (Fig. S20), and the calculated adsorption energy is −2.29 eV (Figs. 12C and 12D), which is smaller than that of pristine CeO_2. The results reveal that the adsorption of SO_2 is weakened on the *x*Cu/Ce catalysts. As a result, the formation of sulfate is hindered and the active sites are preserved, and the Cu-doped CeO_2

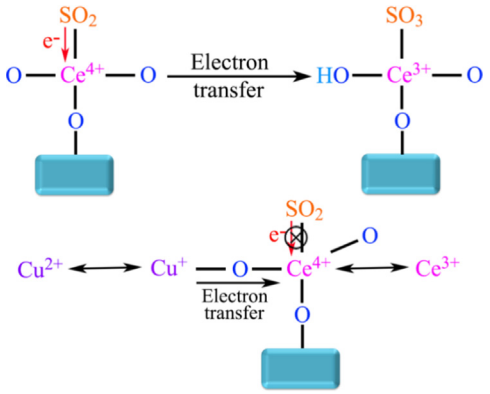

Fig. 13. Schematic of restricted oxidation of SO_2 to SO_3 over Cu-doped CeO_2.

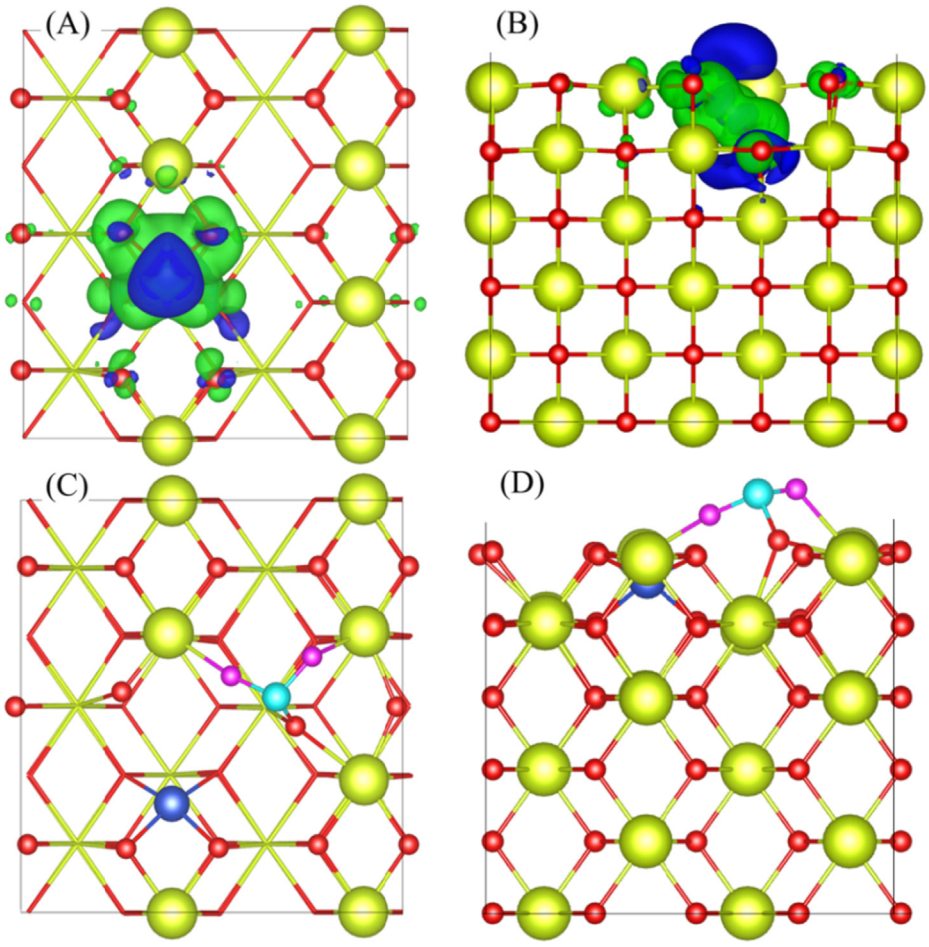

Fig. 12. (A, B) Top and side views of differential charge densities for Cu-doped CeO_2 model (the green color represents the gain of electrons and the blue one indicates the loss of electrons); (C, D) top and side views of the most steady configuration of SO_2 adsorption on the Cu-doped $CeO_{2\text{-}x}$ (110) surface (yellow, Ce; dark blue, Cu; light blue, S; red and pink, O atoms).

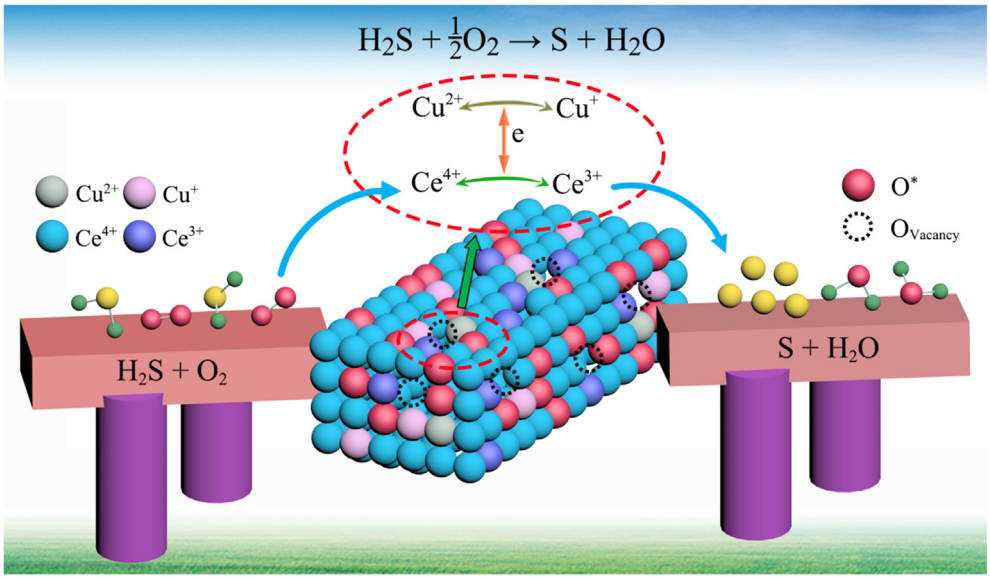

Fig. 14. Diagram of H_2S oxidation over Cu-doped CeO_2 catalyst.

shows high SO_2 resistance and long-term stability. Therefore, a mechanism for the significant SO_2 resistance of Cu-doped CeO_2 can be described as follows (Fig. 13): An electron of SO_2 adsorbed onto CeO_2 transfers to Ce^{4+}, leading to the oxidation of SO_2 to SO_3 and subsequently to sulfate. As for Cu-doped CeO_{2-x}, the transfer of an electron from SO_2 to Ce^{4+} is suppressed by the fact that there is also a transfer of an electron from Cu^+ to Ce^{4+}, and sulfate formation is hence hindered.

Based on the above presentation, a plausible reaction pathway for selective H_2S oxidation on Cu-doped CeO_2 nanorods with well-defined reactive crystal facets is proposed (Fig. 14). A H_2S molecule first diffuses on the catalyst surface, adsorbs onto an oxygen vacancy, and dissociates to give an HS^- ion. The HS^- ion could be oxidized to S by Ce^{4+}, together with the reduction of Ce^{4+} to Ce^{3+} and the release of a surface oxygen vacancy. Concurrently, the electron transfer process leads to the activation of a lattice oxygen, and a Ce^{3+} ion close by is oxidized according to the pathway $Ce^{3+} + Cu^{2+} \leftrightarrow Ce^{4+} + Cu^+$. Finally, the Cu^+ species are reoxidized to Cu^{2+} by chemisorbed oxygen derived from gaseous O_2 ($O_{2(g)} + V_{\ddot{O}} \rightarrow 2O_{(ads)}$) and participate in the reaction again [67]. The other route is that the HS^-/S^{2-} ion interacts with Cu^{2+} to produce S, accompanied by the generation of CuS. Then the CuS can react with O_2 in the feed gases to form sulfur, together with the regeneration of Cu^{2+} ($CuS + 0.5O_2 + 2H^+ = Cu^{2+} + S + H_2O$) [68].

4. Conclusions

In summary, a series of porous Cu-doped CeO_2 nanorods with different copper content were prepared through a facile hydrothermal method, and the effect of the doped copper on the catalytic performance of CeO_2 in selective H_2S oxidation was studied in detail. Among the prepared catalysts, the one with 10 mol.% Cu doping (10Cu/Ce) is the most outstanding, giving H_2S conversion, S selectivity, and sulfur yield close to 100% at 220 °C. The results reveal that the introduction of Cu species results in enhanced generation of oxygen vacancies, strong reducibility, and high surface oxygen mobility, which are beneficial for H_2S selective oxidation. Meanwhile, remarkable catalytic stability is achieved over copper-doped ceria because the Cu ions alleviate ceria deactivation due to sulfation, raising the adoptability of ceria in industrial applications. The DFT calculations suggest that the Cu doping weakens the adsorption of SO_2 on ceria and thus improves the long-term stability of ceria-based catalysts in H_2S oxidation, in agreement with the experimental results. The findings of the present study open up new avenues for the design of efficient catalysts for oxidative desulfurization.

Declaration of Competing Interest

The authors declare that they have no known competing financial interests or personal relationships that could have appeared to influence the work reported in this paper.

Acknowledgments

The authors are grateful for financial support from the National Science Fund for Distinguished Young Scholars of China (21825801), the National Key Research and Development Program of China (2018YFA0209304), the National Natural Science Foundation of China (21773030, 21603034, and 21878052), and the Natural Science Foundation of Fujian Province (2017J05022).

Appendix A. Supplementary material

Supplementary data to this article can be found online at https://doi.org/10.1016/j.jcat.2020.06.010.

References

[1] Y. Pan, M. Chen, M. Hu, M. Tian, Y. Zhang, D. Long, Probing the room-temperature oxidative desulfurization activity of three-dimensional alkaline graphene aerogel, Appl. Catal. B Environ. 262 (2019) 118266.
[2] Y. Cao, X. Zheng, Z. Du, L. Shen, Y. Zheng, C. Au, L. Jiang, Low temperature H_2S removal from gas streams over γ-FeOOH, γ-Fe_2O_3 and α-Fe_2O_3: effects of hydroxyl group, defect and specific surface area, Ind. Eng. Chem. Res. 58 (2019) 19353–19360.
[3] R. Sui, C.B. Lavery, D. Li, C.E. Deering, N. Chou, N.I. Dowling, R.A. Marriott, Improving low-temperature CS_2 conversion for the Claus process by using La (III)-doped nanofibrous TiO_2 xerogel, Appl. Catal. B Environ. 241 (2019) 217–226.
[4] C. Lei, W. Zhou, L. Shen, X. Zheng, Q. Feng, Y. Liu, Y. Lei, S. Liang, D. Zhang, L. Jiang, Enhanced selective H_2S oxidation performance on Mo_2C modified g-C_3N_4, ACS Sust. Chem. Eng. 7 (2019) 16257–16263.
[5] S. Afzal, X. Quan, S. Lu, Catalytic performance and an insight into the mechanism of CeO_2 nanocrystals with different exposed facets in catalytic ozonation of p-nitrophenol, Appl. Catal. B Environ. 248 (2019) 526–537.

[6] F. Zhang, X. Zhang, Z. Hao, G. Jiang, H. Yang, S. Qu, Insight into the H_2S selective catalytic oxidation performance on well-mixed Ce-containing rare earth catalysts derived from MgAlCe layered double hydroxides, J. Hazard. Mater. 342 (2018) 749–757.
[7] V. Palma, D. Barba, H_2S purification from biogas by direct selective oxidation to sulfur on V_2O_5–CeO_2 structured catalysts, Fuel 135 (2014) 99–104.
[8] D.E. Koyuncu, S. Yasyerli, Selectivity and stability enhancement of iron oxide catalyst by ceria incorporation for selective oxidation of H_2S to sulfur, Ind. Eng. Chem. Res. 48 (2009) 5223–5229.
[9] X. Zheng, Y. Li, L. Zhang, L. Shen, Y. Xiao, Y. Zhang, C. Au, L. Jiang, Insight into the effect of morphology on catalytic performance of porous CeO_2 nanocrystals for H_2S selective oxidation, Appl. Catal. B Environ. 252 (2019) 98–110.
[10] L. Shuang, W. Xiaodong, W. Duan, R. Rui, Ceria-based catalysts for soot oxidation: a review, J. Rare Earth 33 (2015) 567–590.
[11] S. Ding, F. Liu, X. Shi, H. He, Promotional effect of Nb additive on the activity and hydrothermal stability for the selective catalytic reduction of NO_x with NH_3 over $CeZrO_x$ catalyst, Appl. Catal. B Environ. 180 (2016) 766–774.
[12] Y. Wang, Z. Chen, P. Han, Y. Du, Z. Gu, X. Xu, G. Zheng, Single-atomic Cu with multiple oxygen vacancies on ceria for electrocatalytic CO_2 reduction to CH_4, ACS Catal. 8 (2018) 7113–7119.
[13] W. Wang, Q. Zhu, Q. Dai, X. Wang, Fe doped CeO_2 nanosheets for catalytic oxidation of 1,2–dichloroethane: Effect of preparation method, Chem. Eng. J. 307 (2017) 1037–1046.
[14] W. Li, Y. Hu, H. Jiang, N. Jiang, W. Bi, C. Li, Litchi-peel-like hierarchical hollow copper-ceria microspheres: aerosol-assisted synthesis and high activity and stability for catalytic CO oxidation, Nanoscale 10 (2018) 22775–22786.
[15] C. Li, Y. Sun, F. Hess, I. Djerdj, J. Sann, P. Voepel, P. Cop, Y. Guo, B.M. Smarsly, H. Over, Catalytic HCl oxidation reaction: stabilizing effect of Zr-doping on CeO_2 nano-rods, Appl. Catal. B Environ. 239 (2018) 628–635.
[16] Q. Xie, H. Zhang, J. Kang, J. Cheng, Q. Zhang, Y. Wang, Oxidative dehydrogenation of propane to propylene in the presence of HCl catalyzed by CeO_2 and NiO-modified CeO_2 nanocrystals, ACS Catal. 8 (2018) 4902–4916.
[17] P. Sudarsanam, B. Hillary, B. Mallesham, B.G. Rao, M.H. Amin, A. Nafady, A.M. Alsalme, B.M. Reddy, S.K. Bhargava, Designing CuO_x nanoparticle-decorated CeO_2 nanocubes for catalytic soot oxidation: Role of the nanointerface in the catalytic performance of heterostructured nanomaterials, Langmuir 32 (2016) 2208–2215.
[18] J. Sun, L. Zhang, C. Ge, C. Tang, L. Dong, Comparative study on the catalytic CO oxidation properties of CuO/CeO_2 catalysts prepared by solid state and wet impregnation, Chin. J. Catal. 35 (2014) 1347–1358.
[19] B. Liu, C. Li, G. Zhang, X. Yao, S.S.C. Chuang, Z. Li, Oxygen vacancy promoting dimethyl carbonate synthesis from CO_2 and methanol over Zr-doped CeO_2 nanorods, ACS Catal. 8 (2018) 10446–10456.
[20] P. Trogadas, J. Parrondo, V. Ramani, CeO_2 surface oxygen vacancy concentration governs in situ free radical scavenging efficacy in polymer electrolytes, ACS Appl. Mater. Interfaces 4 (2012) 5098–5102.
[21] N. Qiu, J. Zhang, Z. Wu, T. Hu, P. Liu, Optical and ferromagnetic properties of hydrothermally synthesized CeO_2/CuO nanocomposites, Ceram. Int. 44 (2018) 5284–5290.
[22] W. Yang, C. Li, H. Wang, X. Li, W. Zhang, H. Li, Cobalt doped ceria for abundant storage of surface active oxygen and efficient elemental mercury oxidation in coal combustion flue gas, Appl. Catal. B Environ. 239 (2018) 233–244.
[23] P. Ratnasamy, D. Srinivas, C. Satyanarayana, P. Manikandan, R.S. Kumaran, M. Sachin, V.N. Shetti, Influence of the support on the preferential oxidation of CO in hydrogen-rich steam reformates over the CuO-CeO_2-ZrO_2 system, J. Catal. 221 (2004) 455–465.
[24] X. Cheng, X. Zhang, D. Su, Z. Wang, J. Chang, C. Ma, NO reduction by CO over copper catalyst supported on mixed CeO_2 and Fe_2O_3: catalyst design and activity test, Appl. Catal. B Environ. 239 (2018) 485–501.
[25] B. Qiu, C. Wang, N. Zhang, L. Cai, Y. Xiong, Y. Chai, CeO_2 induced interfacial Co^{2+} octahedral sites and oxygen vacancies for water oxidation, ACS Catal. 9 (2019) 6484–6490.
[26] H. He, X. Lin, S. Li, Z. Wu, J. Gao, J. Wu, W. Wen, D. Ye, M. Fu, The key surface species and oxygen vacancies in MnO_x(0.4)-CeO_2 toward repeated soot oxidation, Appl. Catal. B Environ. 223 (2018) 134–142.
[27] J. Ma, Y. Lou, Y. Cai, Z. Zhao, L. Wang, W. Zhan, Y. Guo, Y. Guo, The relationship between the chemical state of Pd species and the catalytic activity for methane combustion on Pd/CeO_2, Catal. Sci. Technol. 8 (2018) 2567–2577.
[28] V. Alcalde-Santiago, A. Davó-Quiñonero, D. Lozano-Castelló, A. Bueno-López, On the soot combustion mechanism using 3DOM ceria catalysts, Appl. Catal. B Environ. 234 (2018) 187–197.
[29] L. Du, W. Wang, H. Yan, X. Wang, Z. Jin, Q. Song, R. Si, C. Jia, Copper-ceria sheets catalysts: effect of copper species on catalytic activity in CO oxidation reaction, J. Rare Earth 35 (2017) 1186–1196.
[30] Y. Zheng, K. Li, H. Wang, Y. Wang, D. Tian, Y. Wei, X. Zhu, C. Zeng, Y. Luo, Structure dependence and reaction mechanism of CO oxidation: a model study on macroporous CeO_2 and CeO_2-ZrO_2 catalysts, J. Catal. 344 (2016) 365–377.
[31] H. Shang, X. Zhang, J. Xu, Y. Han, Effects of preparation methods on the activity of CuO/CeO_2 catalysts for CO oxidation, Front. Chem. Sci. Eng. 11 (2017) 603–612.
[32] X. Zheng, X. Chen, J. Chen, Y. Zheng, L. Jiang, Synthesis and application of highly dispersed ordered mesoporous silicon-doped Pd-alumina catalyst with high thermal stability, Chem. Eng. J. 297 (2016) 148–157.
[33] Y. Xiao, X. Zheng, X. Chen, L. Jiang, Y. Zheng, Synthesis of Mg-doped ordered mesoporous Pd-Al_2O_3 with different basicity for CO, NO, and HC elimination, Ind. Eng. Chem. Res. 56 (2017) 1687–1695.
[34] F. Hu, J. Chen, Y. Peng, H. Song, K. Li, J. Li, Novel nanowire self-assembled hierarchical CeO_2 microspheres for low temperature toluene catalytic combustion, Chem. Eng. J. 331 (2018) 425–434.
[35] W. Wang, J.Y. Howe, Y. Li, X. Qiu, D.C. Joy, M.P. Paranthaman, M.J. Doktycz, B. Gu, A surfactant and template-free route for synthesizing ceria nanocrystals with tunable morphologies, J. Mater. Chem. 20 (2010) 7776–7781.
[36] L. Shen, X. Zheng, G. Lei, X. Li, Y. Cao, L. Jiang, Hierarchically porous γ-Al_2O_3 nanosheets: Facile template-free preparation and reaction mechanism for H_2S selective oxidation, Chem. Eng. J. 346 (2018) 238–248.
[37] Z. Wu, M. Li, S.H. Overbury, On the structure dependence of CO oxidation over CeO_2 nanocrystals with well-defined surface planes, J. Catal. 285 (2012) 61–73.
[38] L. Liu, Z. Yao, B. Liu, L. Dong, Correlation of structural characteristics with catalytic performance of CuO/$Ce_xZr_{1-x}O_2$ catalysts for NO reduction by CO, J. Catal. 275 (2010) 45–60.
[39] X.X. Zheng, L.J. Shen, X.P. Chen, X.H. Zheng, C.T. Au, L.L. Jiang, Amino-modified Fe-Terephthalate metal-organic framework as an efficient catalyst for the selective oxidation of H_2S, Inorg. Chem. 57 (2018) 10081–10089.
[40] D. Rickard, G.W. Luther, Chemistry of iron sulfides, Chem. Rev. 107 (2007) 514–562.
[41] X. Zheng, Y. Li, Y. Zheng, L. Shen, Y. Xiao, Y. Cao, Y. Zhang, C.-T. Au, L. Jiang, Highly efficient porous $Fe_xCe_{1-x}O_{2-\delta}$ with three-dimensional hierarchical nanoflower morphology for H_2S-selective oxidation, ACS Catal. 10 (2020) 3968–3983.
[42] S. Liang, J. Mi, F. Liu, Y. Zheng, Y. Xiao, Y. Cao, L. Jiang, Efficient catalytic elimination of COS and H_2S by developing ordered mesoporous carbons with versatile base N sites via a calcination induced self-assembly route, Chem. Eng. Sci. 221 (2020) 115714.
[43] H. Li, S. Liu, J. Yang, Y. Liu, Y. Hu, S. Feng, Z. Yang, J. Zhao, W. Qu, Role of SO_2 and H_2O in the mercury adsorption on ceria surface: a DFT study, Fuel 260 (2020) 116289.
[44] Z. Pi, B. Shen, J. Zhao, J. Liu, CuO, CeO_2 modified Mg-Al spinel for removal of SO_2 from fluid catalytic cracking flue gas, Ind. Eng. Chem. Res. 54 (2015) 10622–10628.
[45] W. Zhao, X. Zheng, S. Liang, X. Zheng, L. Shen, F. Liu, Y. Cao, Z. Wei, L. Jiang, Fe-doped γ-Al_2O_3 porous hollow microspheres for enhanced oxidative desulfurization: facile fabrication and reaction mechanism, Green Chem. 20 (2018) 4645–4654.
[46] G. Djega-Mariadassou, M. Boudart, Classical kinetics of catalytic reactions, J. Catal. 216 (2003) 89–97.
[47] T.K. Ghosh, E.L. Tollefson, Kinetics and reaction mechanism of hydrogen sulfide oxidation over activated carbon in the temperature range of 125–200 °C, Can. J. Chem. Eng. 64 (1986) 969–976.
[48] A.M. Yang, E.L. Tollefson, A.K. Dalai, Oxidation of low concentrations of hydrogen sulphide: process optimization and kinetic studies, Can. J. Chem. Eng. 76 (1998) 76–86.
[49] E. Torres-Garcia, A. Galano, G. Rodriguez-Gattorno, Oxidative desulfurization (ODS) of organosulfur compounds catalyzed by peroxo-metallate complexes of WO_x-ZrO_2: thermochemical, structural, and reactivity indexes analyses, J. Catal. 282 (2011) 201–208.
[50] H.S. Na, J.O. Shim, W.J. Jang, K.W. Jeon, H.M. Kim, Y.L. Lee, D.W. Lee, S.Y. Yoo, J. W. Bae, C.V. Rode, H.S. Roh, The effect of titration time on the catalytic performance of Cu/CeO_2 catalysts for water-gas shift reaction, Catal. Today 309 (2018) 83–88.
[51] J. Mi, Y. Cao, J. Zhang, Y. Ma, C. Chen, D. Li, X. Lin, L. Jiang, Effect of Ce modification on the structural and catalytic property of Co-Mo/Mg(Al)O catalyst for water-gas shift reaction, Appl. Catal. A Gen. 553 (2018) 36–42.
[52] G. Zhou, B. Dai, H. Xie, G. Zhang, K. Xiong, X. Zheng, CeCu composite catalyst for CO synthesis by reverse water-gas shift reaction: effect of Ce/Cu mole ratio, J. CO_2 Util. 21 (2017) 292–301.
[53] M. Konsolakis, The role of Copper-Ceria interactions in catalysis science: recent theoretical and experimental advances, Appl. Catal. B Environ. 198 (2016) 49–66.
[54] X. Zhang, Y. Liu, J. Deng, X. Yu, Z. Han, K. Zhang, H. Dai, Alloying of gold with palladium: an effective strategy to improve catalytic stability and chlorine-tolerance of the 3DOM CeO_2–supported catalysts in trichloroethylene combustion, Appl. Catal. B Environ. 257 (2019) 117879.
[55] Y. Cui, W.-L. Dai, Support morphology and crystal plane effect of Cu/CeO_2 nanomaterial on the physicochemical and catalytic properties for carbonate hydrogenation, Catal. Sci. Technol. 6 (2016) 7752–7762.
[56] X. Yu, L. Wang, M. Chen, X. Fan, Z. Zhao, K. Cheng, Y. Chen, Z. Sojka, Y. Wei, J. Liu, Enhanced activity and sulfur resistance for soot combustion on three-dimensionally ordered macroporous-mesoporous $Mn_xCe_{1-x}O_\delta/SiO_2$ catalysts, Appl. Catal. B Environ. 254 (2019) 246–259.
[57] E. Hayashi, Y. Yamaguchi, K. Kamata, N. Tsunoda, Y. Kumagai, F. Oba, M. Hara, Effect of MnO_2 crystal structure on aerobic oxidation of 5–hydroxymethylfurfural to 2, 5–furandicarboxylic acid, J. Am. Chem. Soc. 141 (2019) 890–900.
[58] X. Zhang, Z. Wang, N. Qiao, S. Qu, Z. Hao, Selective catalytic oxidation of H_2S over well-mixed oxides derived from $Mg_2Al_xV_{1-x}$ layered double hydroxides, ACS Catal. 4 (2014) 1500–1510.
[59] M. Shi, S. Ye, H. Qu, L. Guo, Synergistic effect of Cu^{2+} doping and sulfation in Cu-Ce-S, tolerance to H_2O and SO_2 and decomposition behaviors of ammonia salts, Mol. Catal. 459 (2018) 135–140.
[60] G. Lei, Z. Dai, Z. Fan, X. Zheng, Y. Cao, L. Shen, Y. Xiao, C. Au, L. Jiang, Porous nanosheets of carbon-conjugated graphitic carbon nitride for the oxidation of H_2S to elemental sulfur, Carbon 155 (2019) 204–214.

[61] G. Lei, W. Zhao, L. Shen, S. Liang, C. Au, L. Jiang, Isolated iron sites embedded in graphitic carbon nitride (g-C_3N_4) for efficient oxidative desulfurization, Appl. Catal. B Environ. 267 (2020) 118663.
[62] S. Zhang, C. Zhao, Y. Liu, W. Li, J. Wang, G. Wang, Y. Zhang, H. Zhang, H. Zhao, Cu doping in CeO_2 to form multiple oxygen vacancies for dramatically enhanced ambient N_2 reduction performance, Chem. Commun. 55 (2019) 2952–2955.
[63] A. Omidvar, Catalytic role of transition metals supported on niobium oxide in O_2 activation, Appl. Surf. Sci. 434 (2018) 1239–1247.
[64] S. Zhao, L. Ling, B. Wang, R. Zhang, D. Li, Q. Wang, J. Wang, Theoretic insight into the desulfurization mechanism: removal of H_2S by ceria (110), J. Phys. Chem. C 119 (2015) 7678–7688.
[65] L. Zhang, L. Li, Y. Cao, X. Yao, C. Ge, F. Gao, Y. Deng, C. Tang, L. Dong, Getting insight into the influence of SO_2 on TiO_2/CeO_2 for the selective catalytic reduction of NO by NH_3, Appl. Catal. B Environ. 165 (2015) 589–598.
[66] H. Liu, Z. Fan, C. Sun, S. Yu, S. Feng, W. Chen, D. Chen, C. Tang, F. Gao, L. Dong, Improved activity and significant SO_2 tolerance of samarium modified CeO_2–TiO_2 catalyst for NO selective catalytic reduction with NH_3, Appl. Catal. B Environ. 244 (2019) 671–683.
[67] H. Wang, Z. Qu, H. Xie, N. Maeda, L. Miao, Z. Wang, Insight into the mesoporous $Fe_xCe_{1-x}O_{2-\delta}$ catalysts for selective catalytic reduction of NO with NH_3: Regulable structure and activity, J. Catal. 338 (2016) 56–67.
[68] R. Padilla, P. Pavez, M.C. Ruiz, Kinetics of copper dissolution from sulfidized chalcopyrite at high pressures in H_2SO_4-O_2, Hydrometallurgy 91 (2008) 113–120.